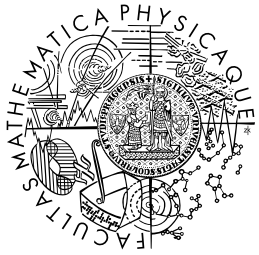


FACULTY
OF MATHEMATICS
AND PHYSICS
Charles University

**BACHELOR THESIS**

David Pokorný

# Impulsive phase of a solar flare and its signatures

Astronomical Institute of Charles University

Supervisor of the bachelor thesis: Mgr. Jana Kašparová, Ph.D.

Study programme: Physics

Prague 2025

I declare that I carried out this bachelor thesis on my own, and only with the cited sources, literature and other professional sources. I understand that my work relates to the rights and obligations under the Act No. 121/2000 Sb., the Copyright Act, as amended, in particular the fact that the Charles University has the right to conclude a license agreement on the use of this work as a school work pursuant to Section 60 subsection 1 of the Copyright Act.

In ..... date .....  .....

Author's signature

I thank my supervisor Jana Kašparová for her patience. She was always very kind and helpful. I thank my consultant Marian Karlický for his insight. I thank Paolo Massa and Shane Maloney for their help with stixpy library. I thank my classmate Vojtěch Votruba for helping me with the formalities.

Title: Impulsive phase of a solar flare and its signatures

Author: David Pokorný

Institute: Astronomical Institute of Charles University

Supervisor: Mgr. Jana Kašparová, Ph.D., Astronomical Institute of the CAS

Consultant: prof. RNDr. Marian Karlický, DrSc., Astronomical Institute of the CAS

Abstract: The solar flares have a typical flux trend with exponential growth and long decay. The growth is caused by sudden intense magnetic energy release and is called the impulsive phase of the solar flare. We aim to tie together various types of the observed electromagnetic emission in order to provide an interpretation of the event from 2021-10-09. We analysed X-ray spectra from STIX and used them to reproject images of X-ray sources over EUV images from AIA. We performed wavelet analysis on radio data from Ondřejov and Learmonth observatories, EUV data from AIA and HXR data from STIX. Our results show two distinct hard X-ray sources corresponding to the flare footpoints. The source located near a sunspot was notably more efficient at accelerating particles to higher energies. We also identified quasi-periodic pulses (QPPs) with matching periods occurring at similar times in both radio and hard X-ray observations.

Keywords: solar flare, X-rays, spectra, EUV emission, images

Název práce: Impulsivní fáze sluneční erupce a její projevy

Autor: David Pokorný

Ústav: Astronomický ústav UK

Vedoucí bakalářské práce: Mgr. Jana Kašparová, Ph.D., Astronomický ústav AV ČR, v. v. i

Konzultant: prof. RNDr. Marian Karlický, DrSc., Astronomický ústav AV ČR, v. v. i

Abstrakt: Tok energie ze slunečních erupcí má typický průběh s exponenciálním vzrůstem a postupným poklesem. Tento vzrůst je způsoben náhlým a prudkým uvolněním magnetické energie a je nazýván impulsivní fáze sluneční erupce. Naším cílem je provázat různé typy pozorované elektromagnetické emise abychom vytvořili konzistentní interpretaci události z 2021-10-09. Analyzovali jsme rentgenová spektra z přístroje STIX a použili je k reprojekci obrazů rentgenových zdrojů na obrázky v EUV z přístroje AIA. Provedli jsme waveletovou analýzu rádiových dat z Ondřejovské a Learmonthské observatoře, EUV dat z AIA a HXR dat ze STIX. Výsledkem naši práce je identifikace dvou rentgenových zdrojů jako ukotvení erupční smyčky. Zdroj v těsné blízkosti sluneční skvrny je značně efektivnější v urychlování částic do vysokých energií. Dále jsme v rádiových a rentgenových datech našli kvazi-periodické pulzace se stejnou periodou v podobný čas.

Klíčová slova: sluneční erupce, rentgenová emise, spektra, EUV emise, obrazová data

# Contents

# 1 Theory

*"Be praised, my Lord, through all your creatures, especially Sir Brother Sun"*

— Francis of Assisi

In this chapter, we introduce key words and theoretical concepts needed for any meaningful discussion of physical reality.

## 1.1 Structure of the Sun

We start by mapping the definitions of the solar structure. As it is a main sequence star of lower mass, its interior can be divided to the core, the radiative zone and the convection zone. In this work, we will focus less on these internal regions and more on the outer layers. Specifically, we turn our attention to the solar atmosphere, which, despite being continuous, is traditionally segmented into discrete layers:

1. Photospehere: This is the visible surface of the Sun, observable without any specialized equipment. It is around 500 km thick. In the photosphere the temperature is decreasing with an increasing distance from the Sun core, with an average around 5700 K, reaching as low as 4100 K. This is the temperature minimum. This layer is where sunspots and granulation patterns form.

2. Chromosphere: It can be observed in Extreme ultraviolet (EUV) and strong emission lines (hence the name). There is little agreement in the literature on its thickness; different sources give vastly different numbers: $10^4$ km [1], 15000 km [2], 1500 km [3], 1500 km [4], 2000 km [5]. However, the higher estimates probably did not now about the existence of the layer above (transition region). However, the idea of layers is still a rough approximation, so the thickness does not have to be exact. The chromosphere is usually defined beginning in the temperature rise just above the temperature minimum region [3].

3. Transition region: it is a thin region where the temperature rises from 20000 K to $10^6$ K in 200 km. It should not be considered a geometrical layer, rather a temperature regime; not only because of the extreme spatial inhomogeneity of this region, but also because of the sharp transition in temperature (and therefore the density as well for pressure must remain continuous) [5].

4. Corona: It is the outermost layer of solar atmosphere. After the rapid rise in transition region the temperature profile flattens and we come to an extended region with the temperature around $10^6$ K. The cause of this high temperature is still unknown.

This section was based on Vanýsek [1], Budějický [2], Stix [5], Shapiro [4], Foukal [3] and Lang [6].

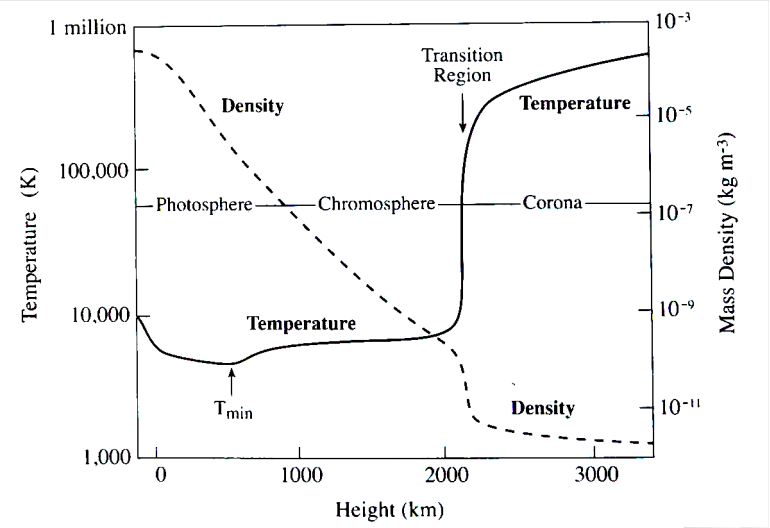


**Figure 1.1** Dependence of temperature and density on the height above the solar surface [6].

## 1.2 Introduction to solar flare physics

The solar flare itself is a result of Magnetohydrodynamic (MHD) processes occurring in the Sun. Let us now introduce a few key concepts.

### 1.2.1 Induction equation

Since the Sun is made of plasma, we will describe it using Maxwell equations in slow variations approximation and with no free charge (Debye shielding) [7]

$$\nabla \cdot \mathbf{E} = 0, \tag{1.1}$$

$$\nabla \cdot \mathbf{B} = 0, \tag{1.2}$$

$$\nabla \times \mathbf{E} = -\frac{\partial \mathbf{B}}{\partial t}, \tag{1.3}$$

$$\nabla \times \mathbf{B} = \mu_0 \mathbf{j}, \tag{1.4}$$

where $\mu_0$ is the permeability of the free space. Concurrently for current density we have

$$\eta_e \mathbf{j} = \mathbf{E} + \mathbf{v} \times \mathbf{B}, \tag{1.5}$$

where $\eta_e$ is the electrical resistivity and $\mathbf{v}$ is the velocity of plasma. For evolution of the magnetic field we get

$$\begin{aligned} \frac{\partial \mathbf{B}}{\partial t} &= -\nabla \times (-\mathbf{v} \times \mathbf{B} + \eta_e \mathbf{j}) = \\ &= \nabla \times (\mathbf{v} \times \mathbf{B}) - \frac{\eta_e}{\mu_0} \nabla \times (\nabla \times \mathbf{B}) = \\ &= \nabla \times (\mathbf{v} \times \mathbf{B}) - \eta \left(\nabla (\nabla \cdot \mathbf{B}) - \nabla \cdot \nabla \mathbf{B}\right) = \\ &= \nabla \times (\mathbf{v} \times \mathbf{B}) - \eta \Delta \mathbf{B}, \end{aligned} \tag{1.6}$$

where $\eta = \frac{\eta_e}{\mu_0}$ is the magnetic diffusivity. This result is known as the induction equation

$$\frac{\partial \mathbf{B}}{\partial t} = \nabla \times (\mathbf{v} \times \mathbf{B}) - \eta \Delta \mathbf{B}. \tag{1.7}$$

It plays a crucial role in the solar flare phenomenon.

This subsection was based on Karlický [7].

### 1.2.2 Alfvén theorem

On larger temporal scales $\eta$ is of negligible size so we get the collisionless form of the induction equation

$$\frac{\partial \mathbf{B}}{\partial t} = \nabla \times (\mathbf{v} \times \mathbf{B}). \tag{1.8}$$

Let us now explore the temporal evolution of the magnetic flux [8]

$$\frac{D\Phi_B}{Dt} = \frac{D}{Dt} \int_{s(t)} \mathbf{B} \cdot \mathrm{d}\mathbf{s}. \tag{1.9}$$

We use Reynolds transport theorem and the definition of material derivative

$$\begin{aligned} \frac{D}{Dt} \int_{s(t)} \mathbf{B} \cdot \mathrm{d}\mathbf{s} &= \int_{s(t)} \left( \frac{D}{Dt}\mathbf{B} + \mathbf{B}\nabla \cdot \mathbf{v} - \mathbf{B} \cdot \nabla \mathbf{v} \right) \cdot \mathrm{d}\mathbf{s} = \\ &= \int_{s(t)} \left( \frac{\partial \mathbf{B}}{\partial t} + \mathbf{v} \cdot \nabla \mathbf{B} + \mathbf{B}\nabla \cdot \mathbf{v} - \mathbf{B} \cdot \nabla \mathbf{v} \right) \cdot \mathrm{d}\mathbf{s}. \end{aligned} \tag{1.10}$$

Now we have to realize the vector identity

$$\nabla \times (\mathbf{v} \times \mathbf{B}) = \mathbf{B} \cdot \nabla \mathbf{v} + \mathbf{v}\nabla \cdot \mathbf{B} - \mathbf{v} \cdot \nabla \mathbf{B} - \mathbf{B}\nabla \cdot \mathbf{v}. \tag{1.11}$$

If we substitute from the collisionless induction equation 1.8 and use Gauss's law 1.2 we get

$$\begin{aligned} &\nabla \times (\mathbf{v} \times \mathbf{B}) + \mathbf{v} \cdot \nabla \mathbf{B} + \mathbf{B}\nabla \cdot \mathbf{v} - \mathbf{B} \cdot \nabla \mathbf{v} = \\ &= \mathbf{B} \cdot \nabla \mathbf{v} + \mathbf{v}\nabla \cdot \mathbf{B} - \mathbf{v} \cdot \nabla \mathbf{B} - \mathbf{B}\nabla \cdot \mathbf{v} + \mathbf{v} \cdot \nabla \mathbf{B} + \mathbf{B}\nabla \cdot \mathbf{v} - \mathbf{B} \cdot \nabla \mathbf{v} = \\ &= \mathbf{B} \cdot \nabla \mathbf{v} - \mathbf{B} \cdot \nabla \mathbf{v} - \mathbf{v} \cdot \nabla \mathbf{B} + \mathbf{v} \cdot \nabla \mathbf{B} - \mathbf{B}\nabla \cdot \mathbf{v} + \mathbf{B}\nabla \cdot \mathbf{v} = \\ &= 0. \end{aligned} \tag{1.12}$$

Therefore, the magnetic flux is conserved.

$$\frac{D\Phi_B}{Dt} = \int_{s(t)} 0 \cdot \mathrm{d}\mathbf{s} = 0. \tag{1.13}$$

This is the Alfvén theorem. It tells us that the magnetic field "freezes in" the plasma.

This subsection was inspired by Karlický [7] and Kulhánek [8].

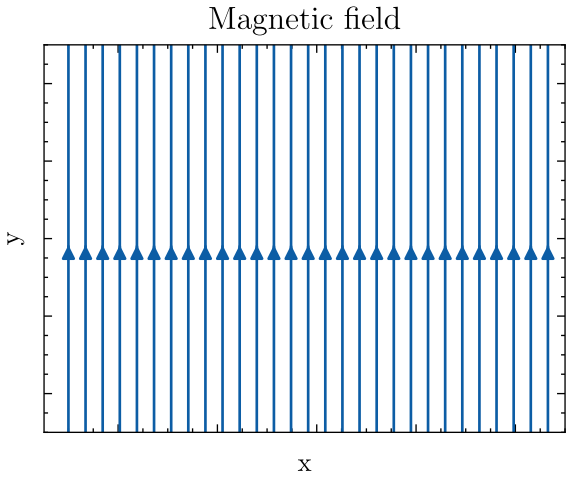


**Figure 1.2** Initial homogeneous magnetic field

### 1.2.3 The impulsive phase

Let us now investigate a simple example. We begin with a homogeneous magnetic field, as shown in Figure 1.2. This can serve as a naive approximation of either the quiet Sun atmosphere (facing the edge of the Sun). The magnetic field is assumed to be in a region of plasma where the Alfvén theorem applies. For some reason — such as convection — the plasma begins to move, but in a spatially non-uniform way. In our example, the velocity field is very simple

$$v_x \sim \exp\left(-x^2\right) \exp\left(-y^2\right) \tag{1.14}$$

compare with Figure 1.3 . Now we can rewrite the equation 1.8 using the material

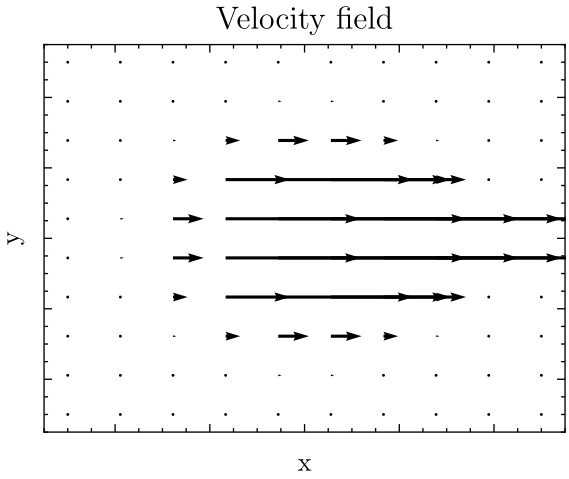


**Figure 1.3** Non-uniform plasma velocity vector field causing the stretch of the magnetic field lines

derivative [8]

$$\frac{D\mathbf{b}}{Dt} = \mathbf{b} \cdot \nabla \mathbf{v} \tag{1.15}$$

where $\mathbf{b} = \frac{\mathbf{B}}{\rho}$. For our simple field we get

$$\frac{Db_x}{Dt} = b_y \frac{\partial v_x}{\partial y} \tag{1.16}$$

and if we let our field evolve[1] we get something similar to what we see in Figure 1.4. This shape can already remind us of the magnetic arcades that can be observed

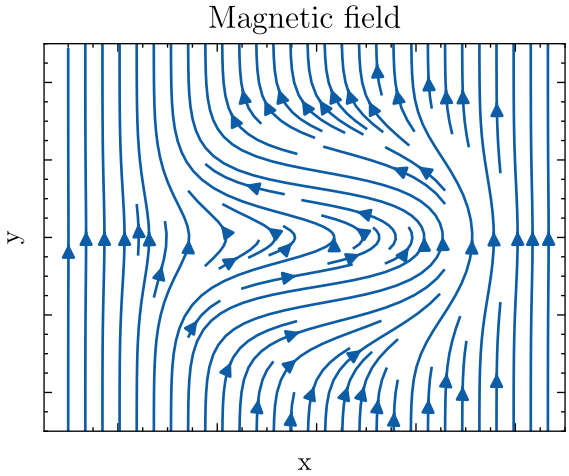


**Figure 1.4** Magnetic field stretched by the motion of the plasma in the positive x-axis direction. The magnetic flux is conserved due to Alfvén theorem 1.13

on the solar surface. Let us now recall what is the result of such a configuration of magnetic lines; because of Ampere's law 1.4, current arises in the region beneath the arcades. The curl of the magnetic field 1.4 is in Figure 1.5. This is called

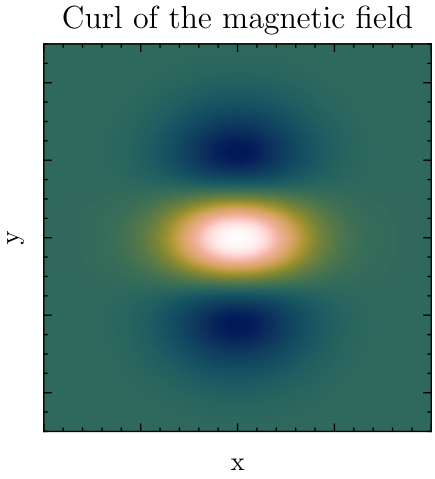


**Figure 1.5** Intensity of a curl of the magnetic field in Figure 1.4 corresponds directly with current density via Amperes law 1.4

current sheet and its formation leads to the magnetic reconnection itself.

Let us now imagine a scenario where, for some reason, the magnetic diffusivity increases drastically in the current sheet. Let the length of this diffusion region

[1]The authors implementation of this is far from proper. However, since this is no important result but only an illustration, he is not ashamed of it.

be $2L$ and its width $2l$. We further assume that the magnitude of the magnetic field is $B_i$. Since the current is perpendicular to the magnetic field lines, it begins to exert a force on the plasma through the attractive Lorentz force.

$$\mathbf{F} = \mathbf{j} \times \mathbf{B}. \tag{1.17}$$

This causes the plasma to move to the diffusion region, dragging the field lines with it at velocity $v_i$. The mass conservation implies that on the shorter sides $2l$ there must be a plasma outflow of velocity $v_0$such that

$$Lv_i = lv_0. \tag{1.18}$$

This plasma drags away reconnected field lines with magnitude $B_0$. This is illustrated in Figure 1.6

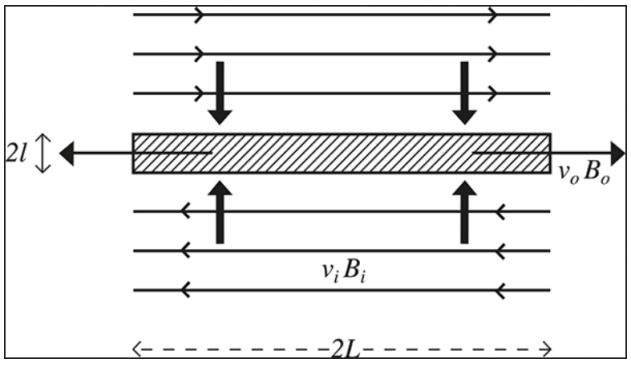


**Figure 1.6** Scheme of the Sweet-Parker model [9]. The field lines are dragged into the diffusion region when reconnection takes place pushing the plasma out of it.

We will now find these velocities.

1. The initial velocity of the plasma must be equal to the velocity of the diffusion determined by the so called resistive timescale $\tau_R$

$$v_i = \frac{l}{\tau_R} = \frac{\eta}{l}, \tag{1.19}$$

where $\eta$ is the magnetic diffusivity.

2. The outflow velocity results from the acceleration generated by the Lorentz force acting on the matter at rest at the center of the current sheet (the stagnation point). If we associate this with the magnetic pressure, we obtain

$$\rho v_0 \frac{\partial v_x}{\partial x} = \rho \frac{v_0^2}{L} \approx \frac{B_i B_0}{\mu l}, \tag{1.20}$$

where $\rho$ is the density of the plasma and $\mu$ is its permeability. From Gauss' law we get

$$\frac{B_0}{l} = \frac{B_i}{L}, \tag{1.21}$$

so for the outflow velocity we find

$$v_0^2 = \frac{B_i^2}{\mu\rho}. \tag{1.22}$$

The outcome of magnetic reconnection is illustrated in Figure 1.7. As we can observe, the magnetic arcade from Figure 1.4 becomes narrower at the current sheet. The inflow and outflow dynamics give rise to post-flare loops and filament matter. This process leads to the release of magnetic energy. But what is the energy balance? Let us now illustrate this on a Sweet-Parker model. The magnetic

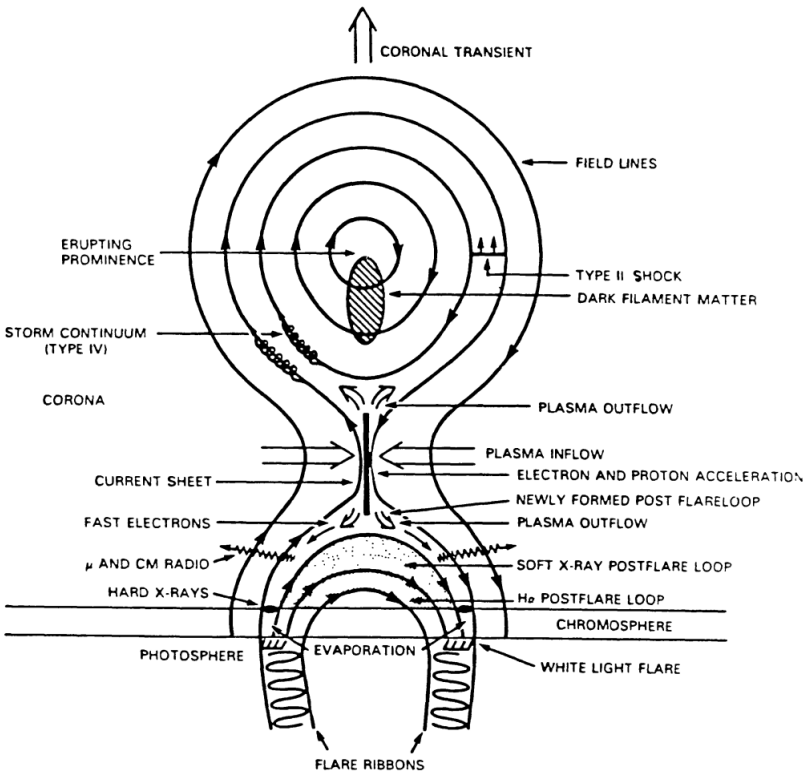


**Figure 1.7** Field lines in a 2 dimensional model of a solar flare [10]. The reconnection takes place at the current sheet.

energy density is

$$u_m = \frac{B_i^2}{\mu} \tag{1.23}$$

and the kinetic energy density is

$$u_k = \frac{1}{2}\rho v_i^2. \tag{1.24}$$

Again, due to Alfvén theorem, both the field lines and the plasma has the same inflow velocity, therefore, we can define energy inflow quotient as

$$Q_{K/M}^{in} = \frac{\rho v_i^2 \mu}{2B_i^2} = \frac{v_i^2}{2v_0^2}, \tag{1.25}$$

but from equations 1.18 and 1.21 we know that

$$v_0 B_0 = v_i B_i, \tag{1.26}$$

but $B_i \gg B_0$ so $Q_{K/M}^{in} \ll 1$; in other words the energy flowing in the diffusion region is mostly magnetic. Similarly, for the ratio of inflow of magnetic energy

and outflow of the kinetic we get

$$Q_{K/M}^{out} = \frac{v_0^2}{2v_0^2} = \frac{1}{2}, \tag{1.27}$$

so half of the incoming magnetic energy is transformed to particle kinetic energy. The other half is transformed into thermal energy with the typical released energy flux around $10^{20}$ W [2]. This is the simplest model available; a more accurate approach would require incorporating shock waves, as done in models like the Petschek model, which we will not explore further here. Until now we discussed the equations, but how do they manifest physically?

As mentioned earlier, the matter aligned along the field lines of the arcade beneath the current sheet forms what is known as the flare loop. In our simplified model, the flare loop resembles a half-torus, with the other half submerged below the photosphere. The locations where the loop intersects the photosphere are referred to as footpoints or flare ribbons and have opposite magnetic polarity. During magnetic reconnection, thermal energy is deposited near the top of the flare loop, where the plasma is heated, producing Soft X-ray (SXR) and EUV emissions. At the same time, kinetic energy (nonthermal) appears in the form of accelerated charged particles, as illustrated in Figure 1.8. These charged particles

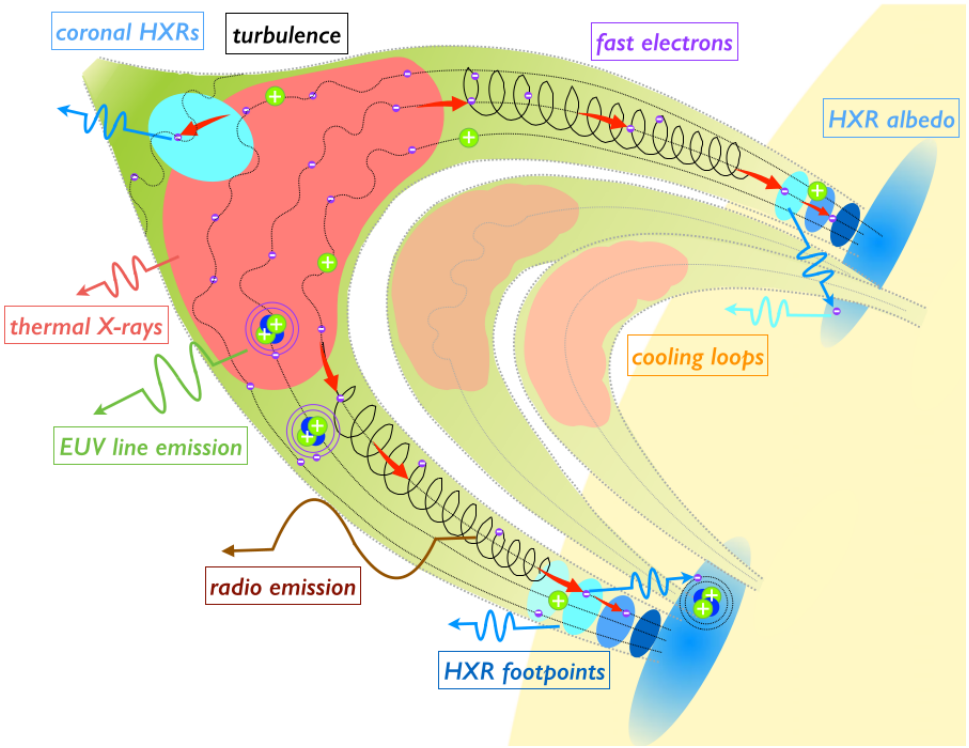


**Figure 1.8** Different kinds of electromagnetic emission caused by magnetic energy release and its conversion into thermal and nonthermal energy [11]

then spiral downward along magnetic field lines with energies as high as hundreds of keV. Their gyration produces radio emission, and as they collide with the dense layers of the photosphere, they lose energy primarily through bremsstrahlung

[2]This value can be found here: `https://hesperia.gsfc.nasa.gov/sftheory//flare.htm?utm_source=chatgpt.com`

(braking radiation). A portion of this radiation is reflected off the photosphere and escapes into space. Thus, although the exact processes in the diffusion region during the impulsive phase cannot be directly observed, the associated phenomena provide us with a rich diagnostics.

This subsection was based on Karlický [7] and Kulhánek [8].

## 1.3 X-ray emission

Given the preceding discussion, it is clear that the impulsive phase involves numerous high-energy phenomena. Keeping the Planck relation in mind, it is not surprising that these would manifest at short wavelengths. The bulk of our analysis is based on X-ray emission, which we will now delve into.

### 1.3.1 Thermal emission

Let us consider a volume $V$, containing a constant density $n_e$ of hot electrons. We assume that their speed distribution $f(v)$ follows a Maxwellian form

$$f(v) = 4\pi \left(\frac{m_e}{2\pi k_B T}\right)^{\frac{3}{2}} n_e v^2 \exp\left(\frac{-m_e v^2}{2k_B T}\right), \tag{1.28}$$

where $m_e$ is the mass of electron, $k_B$ is the Boltzmann constant, $T$ is temperature and $v$ is the speed of electrons. For corresponding energy distribution we have

$$F(E)\,\mathrm{d}E = f(v)\,\mathrm{d}v, \tag{1.29}$$

for the differential we find (assuming non-relativistic energies)

$$\mathrm{d}v = \frac{1}{\sqrt{2m_e E}}\mathrm{d}E, \tag{1.30}$$

thus

$$F(E) = \frac{2n_e}{\sqrt{\pi\left(k_B T\right)^3}}\sqrt{E}\exp\left(-\frac{E}{k_B T}\right), \tag{1.31}$$

These thermal electrons produce bremsstrahlung interacting with ambient protons of the same density $n_p = n_e$. We will derive the resulting flux of photons $I$ as a function of the energy of the photons $\varepsilon$ as

$$I(\varepsilon) = n_e V \int_{\varepsilon}^{\infty} F(E)\, v(E)\, \sigma_B(\varepsilon, E)\,\mathrm{d}E, \tag{1.32}$$

where $\sigma_B$ is the Bethe-Heitler cross-section for bremsstrahlung. The flux of photons $I$ with the units of photons $\mathrm{s}^{-1}$ $\mathrm{J}^{-1}$ is the subject of the latter spectral analysis.

Substituting to the equation we get

$$I(\varepsilon) = n_e V \int_\varepsilon^\infty \frac{2n_e}{\sqrt{\pi (k_B T)^3}} \sqrt{E} \exp\left(-\frac{E}{k_B T}\right) \cdot \\ \cdot \sqrt{\frac{2E}{m}} \frac{8\alpha}{3} r_0^2 \frac{m_e c^2 \overline{Z^2}}{\varepsilon E} \ln\left(\frac{1+\sqrt{1-\frac{\varepsilon}{E}}}{1-\sqrt{1-\frac{\varepsilon}{E}}}\right) \mathrm{d}E = \\ = \sqrt{\frac{8}{\pi m (k_B T)^3}} \frac{8\alpha}{3} r_0^2 \frac{m_e c^2 \overline{Z^2}}{\varepsilon} n_e^2 V \int_\varepsilon^\infty \exp\left(-\frac{E}{k_B T}\right) \ln\left(\frac{1+\sqrt{1-\frac{\varepsilon}{E}}}{1-\sqrt{1-\frac{\varepsilon}{E}}}\right) \mathrm{d}E. \tag{1.33}$$

Where $\alpha$ is the fine structure constant, $r_0$ is the classical electron radius, $m_e$ is the electron mass, $c$ is the speed of light, $\overline{Z^2}$ is the abundance-weighted value of $Z$. For simplicity, let us put all the constants into one and introduce the emission measure $Q = n_e^2 V$. Let us now simplify the integral using substitution

$$I(\varepsilon) = K \frac{Q}{\varepsilon T^{3/2}} \int_\varepsilon^\infty \exp\left(-\frac{E}{k_B T}\right) \ln\left(\frac{1+\sqrt{1-\frac{\varepsilon}{E}}}{1-\sqrt{1-\frac{\varepsilon}{E}}}\right) \mathrm{d}E \Bigg/ \begin{matrix} x = \frac{E}{\varepsilon} - 1 \\ \mathrm{d}x = \frac{\mathrm{d}E}{\varepsilon} \end{matrix} \Bigg/ = \\ = K \frac{Q}{\varepsilon T^{3/2}} \int_0^\infty \exp\left(-\frac{\varepsilon(1+x)}{k_B T}\right) \ln\left(\frac{1+\sqrt{1-\frac{1}{1+x}}}{1-\sqrt{1-\frac{1}{1+x}}}\right) \varepsilon \mathrm{d}x = \\ = K \frac{Q}{T^{3/2}} \exp\left(-\frac{\varepsilon}{k_B T}\right) \int_0^\infty \exp\left(-\frac{\varepsilon x}{k_B T}\right) \ln\left(\frac{1+\sqrt{\frac{1+x-1}{1+x}}}{1-\sqrt{\frac{1+x-1}{1+x}}}\right) \mathrm{d}x. \tag{1.34}$$

We solve this integral by parts

$$I(\varepsilon) = \int_0^\infty \exp\left(-\frac{\varepsilon x}{k_B T}\right) \ln\left(\frac{1+\sqrt{\frac{x}{1+x}}}{1-\sqrt{\frac{x}{1+x}}}\right) \mathrm{d}x = \\ = \left[-\frac{k_B T}{\varepsilon} \exp\left(-\frac{\varepsilon x}{k_B T}\right) \ln\left(\frac{1+\sqrt{\frac{x}{1+x}}}{1-\sqrt{\frac{x}{1+x}}}\right) \mathrm{d}x\right]_0^\infty + \\ + \int_0^\infty \frac{k_B T}{\varepsilon} \exp\left(-\frac{\varepsilon x}{k_B T}\right) \frac{\mathrm{d}}{\mathrm{d}x} \ln\left(\frac{1+\sqrt{\frac{x}{1+x}}}{1-\sqrt{\frac{x}{1+x}}}\right) \mathrm{d}x, \tag{1.35}$$

but the first term on the right hand-side vanishes at both limits. Let us solve the derivative first

$$\frac{\mathrm{d}}{\mathrm{d}x} \ln\left(\frac{1+\sqrt{\frac{x}{1+x}}}{1-\sqrt{\frac{x}{1+x}}}\right) = \frac{1-\sqrt{\frac{x}{1+x}}}{1+\sqrt{\frac{x}{1+x}}} \frac{1-\sqrt{\frac{x}{1+x}}+1+\sqrt{\frac{x}{1+x}}}{\left(1-\sqrt{\frac{x}{1+x}}\right)^2} \frac{\mathrm{d}}{\mathrm{d}x} \sqrt{\frac{x}{1+x}} = \\ = \frac{2}{1-\frac{x}{1+x}} \frac{1}{2\sqrt{x(1+x)^3}} = \frac{1}{\frac{1}{1+x}} \frac{1}{\sqrt{x(1+x)^3}} = \\ = \frac{1}{\sqrt{x(1+x)}}. \tag{1.36}$$

So we get

$$I(\varepsilon) = K\frac{Q}{T^{3/2}}\exp\left(-\frac{\varepsilon}{k_BT}\right)\int_0^\infty \frac{k_BT}{\varepsilon}\exp\left(-\frac{\varepsilon x}{k_BT}\right)\frac{1}{\sqrt{x(1+x)}}\mathrm{d}x = \\ = K'\frac{Q}{\varepsilon T^{1/2}}\exp\left(-\frac{\varepsilon}{k_BT}\right)\int_0^\infty \exp\left(-\frac{\varepsilon x}{k_BT}\right)\frac{1}{\sqrt{x(1+x)}}\mathrm{d}x. \tag{1.37}$$

But for $\frac{\varepsilon}{k_BT} \gg 1$ the integrand behaves like Dirac delta function $\delta(x)$, therefore we can write

$$I(\varepsilon) \doteq K'\frac{Q}{\varepsilon T^{1/2}}\exp\left(-\frac{\varepsilon}{k_BT}\right) = \frac{16\alpha m_e\overline{Z^2}}{3}(r_0c)^2\sqrt{\frac{8}{\pi m k_B}}\frac{Q}{\varepsilon T^{1/2}}\exp\left(-\frac{\varepsilon}{k_BT}\right). \tag{1.38}$$

This type of emission we typically see on SXR wavelengths.

This subsection was based on Tandberg-Hanssen [12].

### 1.3.2 Non-thermal emission

Let us derive the expression for Hard X-ray (HXR) flux $I(\varepsilon)$ (photons $\mathrm{s}^{-1}$ $\mathrm{J}^{-1}$). This flux is caused by accelerated electrons with energy distributed as $F(E_0)$ (electrons $\mathrm{s}^{-1}$ $\mathrm{keV}^{-1}$) losing their energy in area $S$ in solar atmosphere by bremsstrahlung radiation and Coulomb collisions. This is approach is called the thick target model as all the electrons are eventually stopped in the Bremsstrahlung source. In thin target no significant modification to the injected spectrum occurs. According to Tandberg-Hanssen we get

$$I(\varepsilon) = \int_\varepsilon^\infty F(E_0)\, n_\gamma(\varepsilon, E_0)\,\mathrm{d}E_0, \tag{1.39}$$

where $n_\gamma(\varepsilon, E_0)$is the number of photons emitted by unit energy, centered on $\varepsilon$, by an electron of initial energy $E_0$. Number of photons emitted by single electron is identical to number of its interactions. But the electron is losing its energy, therefore we need to integrate

$$n_\gamma(\varepsilon, E_0) = \int_{t_1(E=E_0)}^{t_2(E=\varepsilon)} n_p(t)\,\sigma_B(\varepsilon, E(t))\,v(E(t))\,\mathrm{d}t. \tag{1.40}$$

But for Coulomb collisions we have

$$\frac{\mathrm{d}E}{\mathrm{d}t} = -\sigma_C(E)\,n_p v(E)\,E, \tag{1.41}$$

where $E$ is the energy of electron, $\sigma_C$ is the cross-section for Coulomb collisions, $n_p$ is the density of protons and $v$ is the velocity of the electron. Now we may substitute

$$n_\gamma(\varepsilon, E_0) = \int_\varepsilon^{E_0}\frac{\sigma_B(\varepsilon, E)}{\sigma_C(E)}\frac{\mathrm{d}E}{E}. \tag{1.42}$$

Now we can substitute into the general form 1.39

$$I(\varepsilon) = \int_\varepsilon^\infty F(E_0)\int_\varepsilon^{E_0}\frac{\sigma_B(\varepsilon, E)}{\sigma_C(E)}\frac{\mathrm{d}E}{E}\mathrm{d}E_0, \tag{1.43}$$

and after considering that for the cross-sections we have

$$\sigma_B(\varepsilon, E) = \frac{8\alpha}{3} r_0^2 \frac{m_e c^2 \overline{Z^2}}{\varepsilon E} \ln\left(\frac{1+\sqrt{1-\frac{\varepsilon}{E}}}{1-\sqrt{1-\frac{\varepsilon}{E}}}\right), \tag{1.44}$$

$$\sigma_C(E) = \frac{2\pi e^4}{E^2} \ln(\Lambda), \tag{1.45}$$

where $\alpha$ is the fine structure constant, $r_0$ is the classical electron radius, $m_e$ is the electron mass, $c$ is the speed of light, $\overline{Z^2}$ is the abundance-weighted value of $Z$, $e$ is the elementary charge and $\ln(\Lambda)$ is the Coulomb logarithm, we get

$$\begin{aligned} I(\varepsilon) &= \int_\varepsilon^\infty F(E_0) \cdot \\ &\cdot \int_\varepsilon^{E_0} \frac{8\alpha}{3} r_0^2 \frac{m_e c^2 \overline{Z^2}}{\varepsilon E} \ln\left(\frac{1+\sqrt{1-\frac{\varepsilon}{E}}}{1-\sqrt{1-\frac{\varepsilon}{E}}}\right) \left(\frac{2\pi e^4}{E^2}\ln(\Lambda)\right)^{-1} \frac{\mathrm{d}E}{E}\mathrm{d}E_0 = \\ &= \frac{8\alpha}{3} r_0^2 \frac{m_e c^2 \overline{Z^2}}{\varepsilon} \frac{1}{2\pi e^4 \ln(\Lambda)} \int_\varepsilon^\infty F(E_0) \int_\varepsilon^{E_0} \ln\left(\frac{1+\sqrt{1-\frac{\varepsilon}{E}}}{1-\sqrt{1-\frac{\varepsilon}{E}}}\right) \mathrm{d}E\mathrm{d}E_0 = \\ &= \frac{\alpha m_e \overline{Z^2}}{3\varepsilon \ln(\Lambda)} \left(\frac{c r_0}{\pi e^2}\right)^2 \int_\varepsilon^\infty F(E_0) \int_\varepsilon^{E_0} \ln\left(\frac{1+\sqrt{1-\frac{\varepsilon}{E}}}{1-\sqrt{1-\frac{\varepsilon}{E}}}\right) \mathrm{d}E\mathrm{d}E_0. \end{aligned} \tag{1.46}$$

Let us now assume that the energy distribution is in a form of a power-law.

$$F(E_0) = K_1 E_0^{-\delta}, \tag{1.47}$$

where $K_1$ is some constant and

$$K_2 = \frac{\alpha m_e \overline{Z^2} K_1}{3\varepsilon \ln(\Lambda)} \left(\frac{c r_0}{\pi e^2}\right)^2. \tag{1.48}$$

Now we want to solve the integral

$$K_2 \int_\varepsilon^\infty E_0^{-\delta} \int_\varepsilon^{E_0} \ln\left(\frac{1+\sqrt{1-\frac{\varepsilon}{E}}}{1-\sqrt{1-\frac{\varepsilon}{E}}}\right) \mathrm{d}E\mathrm{d}E_0. \tag{1.49}$$

First we reverse the order of integration

$$\begin{aligned} I(\varepsilon) &= K_2 \int_\varepsilon^\infty E_0^{-\delta} \int_\varepsilon^{E_0} \ln\left(\frac{1+\sqrt{1-\frac{\varepsilon}{E}}}{1-\sqrt{1-\frac{\varepsilon}{E}}}\right) \mathrm{d}E\mathrm{d}E_0 = \\ &= K_2 \int_\varepsilon^\infty \ln\left(\frac{1+\sqrt{1-\frac{\varepsilon}{E}}}{1-\sqrt{1-\frac{\varepsilon}{E}}}\right) \mathrm{d}E \int_E^\infty E_0^{-\delta}\mathrm{d}E_0 = \\ &= K_2 \int_\varepsilon^\infty \frac{E^{1-\delta}}{\delta-1} \ln\left(\frac{1+\sqrt{1-\frac{\varepsilon}{E}}}{1-\sqrt{1-\frac{\varepsilon}{E}}}\right) \mathrm{d}E \end{aligned} \tag{1.50}$$

Now we evaluate by parts

$$\begin{aligned} I(\varepsilon) &= \frac{K_2}{\delta-1}\int_\varepsilon^\infty E^{1-\delta}\ln\left(\frac{1+\sqrt{1-\frac{\varepsilon}{E}}}{1-\sqrt{1-\frac{\varepsilon}{E}}}\right)\mathrm{d}E = \\ &= \frac{K_2}{\delta-1}\left[\frac{E^{2-\delta}}{\delta-2}\ln\left(\frac{1+\sqrt{1-\frac{\varepsilon}{E}}}{1-\sqrt{1-\frac{\varepsilon}{E}}}\right)\mathrm{d}E\right]_\infty^\epsilon + \\ &+ \frac{K_2}{\delta-1}\int_\varepsilon^\infty \frac{E^{2-\delta}}{\delta-2}\frac{\mathrm{d}}{\mathrm{d}E}\ln\left(\frac{1+\sqrt{1-\frac{\varepsilon}{E}}}{1-\sqrt{1-\frac{\varepsilon}{E}}}\right)\mathrm{d}E. \end{aligned} \tag{1.51}$$

But the first term is zero at both limits. Thus we solve

$$\begin{aligned} I(\varepsilon) &= \frac{K_2}{(\delta-2)(\delta-1)}\int_\varepsilon^\infty \frac{E^{2-\delta}}{E\sqrt{1-\frac{\varepsilon}{E}}}\mathrm{d}E = \\ &= \frac{K_2}{(\delta-2)(\delta-1)}\int_\varepsilon^\infty \frac{E^{1-\delta}}{\sqrt{1-\frac{\varepsilon}{E}}}\mathrm{d}E \;\Big/\; \begin{matrix} x=\frac{\varepsilon}{E} \\ \mathrm{d}x=-\frac{\varepsilon}{E^2}\mathrm{d}E \end{matrix} \Big/ = \\ &= -\frac{K_2}{(\delta-2)(\delta-1)}\int_1^0 \frac{x^{\delta-3}}{\sqrt{1-x}}\frac{\varepsilon^{3-\delta}}{\varepsilon}\mathrm{d}x = \\ &= \frac{K_2\varepsilon^{2-\delta}}{(\delta-2)(\delta-1)}\int_0^1 x^{\delta-3}(1-x)^{-1/2}\,\mathrm{d}x. \end{aligned} \tag{1.52}$$

But this is known integral

$$B(a,b) = \int_0^1 x^{a-1}(1-x)^{b-1}\,\mathrm{d}x, \tag{1.53}$$

so we get

$$\begin{aligned} I(\varepsilon) &= \frac{K_2\varepsilon^{2-\delta}}{(\delta-2)(\delta-1)}B\left(\delta-2,\frac{1}{2}\right) = \\ &= \frac{\alpha m_e\overline{Z^2}K_1}{3\ln(\Lambda)}\left(\frac{cr_0}{\pi e^2}\right)^2\frac{B\left(\delta-2,\frac{1}{2}\right)}{(\delta-2)(\delta-1)}\varepsilon^{1-\delta}. \end{aligned} \tag{1.54}$$

We observe that the photon flux also follows a power-law distribution, which, as we will show, aligns well with contemporary measurements.

This subsection was based on Tandberg-Hanssen [12].

### 1.3.3 Albedo

We have established two primary sources of radiation that originate in a solar flare. But this radiation does not travel solely to the observer; it is in fact quite the contrary. What happens to the light that travels towards the Sun? Some part is absorbed, but some is scattered back via Thomson and Compton scattering (see Figure 1.8). The cross section of this interaction is described by Klein-Nishina formula

$$\frac{\mathrm{d}\sigma_c}{\mathrm{d}\Omega}(\varepsilon_0,\theta_s,\Theta) = \frac{1}{4}r_0^2\left(\frac{\varepsilon}{\varepsilon_0}\right)^2\left(\frac{\varepsilon_0}{\varepsilon}+\frac{\varepsilon}{\varepsilon_0}-2+4\cos^2\Theta\right), \tag{1.55}$$

where $\theta_s$ is the scattering angle, $\Theta$ is the angle between the directions of polarization of the initial photon and the final photon and $\varepsilon_0$ and $\varepsilon$ are the initial and final photon energies related by

$$\varepsilon = \frac{\varepsilon_0}{1 + \frac{\varepsilon_0}{mc^2}\left(1 - \cos\theta_s\right)}, \tag{1.56}$$

But it would we very awkward to even try to use these formula to get an analytical solution; we would have to calculate every interaction of photons with electrons in space and time.

Let us take a step back and not think about individual interacting particles but rather primary and secondary photon spectrum $I_p$ and $I_s$

$$I_s\left(\varepsilon\right) = \int_{\varepsilon}^{\varepsilon_{max}} I_p\left(\varepsilon_0\right) G\left(\mu, \varepsilon, \varepsilon_0\right) \mathrm{d}\varepsilon_0, \tag{1.57}$$

where $G\left(\mu, \varepsilon, \varepsilon_0\right)$ is the probability that a photon of initial energy $\varepsilon_0$ incident on a plan-parallel atmosphere is re-emitted in direction $\mu = \cos\theta$ where $\theta$ is the heliocentric angle with energy $\varepsilon$. We call it a Greens function (although it is not solution to any differential equation) and we require

$$1 = \int_0^1 \int_{\varepsilon}^{\varepsilon_{max}} G\left(\mu, \varepsilon, \varepsilon_0\right) \mathrm{d}\varepsilon_0 \mathrm{d}\mu. \tag{1.58}$$

If we find such function, we can write for the measured spectrum

$$I\left(\varepsilon\right) = I_p\left(\varepsilon\right) + \int_{\varepsilon}^{\varepsilon_{max}} I_p\left(\varepsilon_0\right) G\left(\mu, \varepsilon, \varepsilon_0\right) \mathrm{d}\varepsilon_0, \tag{1.59}$$

which we have yet to invert to get what we want, but we should see now why we need the $G$. Again, there is no way to derive the equation for $G$ analytically; instead Monte Carlo simulations of the interactions have been done and then the results have been fitted [13]. Examples for three different initial energies and of such a function is in Figure 1.9[3]. The idea is that it will be much faster to look up the corrections from the database instead of calculating them over and over. In reality, we measure on discrete scales, the integrals transforms to a sum

$$I\left(\varepsilon_i\right) = I_p\left(\varepsilon_i\right) + I_p\left(\varepsilon_j\right) G_{ij}\left(\mu\right), \tag{1.60}$$

where

$$G_{ij}\left(\mu\right) = \int_{\varepsilon_j}^{\varepsilon_{j+1}} G\left(\mu, \varepsilon_i, \varepsilon_0\right) \mathrm{d}\varepsilon_0 \tag{1.61}$$

is the Greens matrix. Now we invert the equation 1.60

$$I_p\left(\varepsilon_j\right) = \left(E_{ij} + \alpha G_{ij}\right)^{-1} I\left(\varepsilon_i\right), \tag{1.62}$$

where $E_{ij}$ is the identity matrix and $\alpha$ is additional anisotropy parameter. We assumed that the radiation is isotropic, which means that $\alpha = 1$ is a constant.

This subsection was based on Kontar et al. [14].

[3]These functions are available at `https://hesperia.gsfc.nasa.gov/ssw/packages/xray/dbase/albedo/`

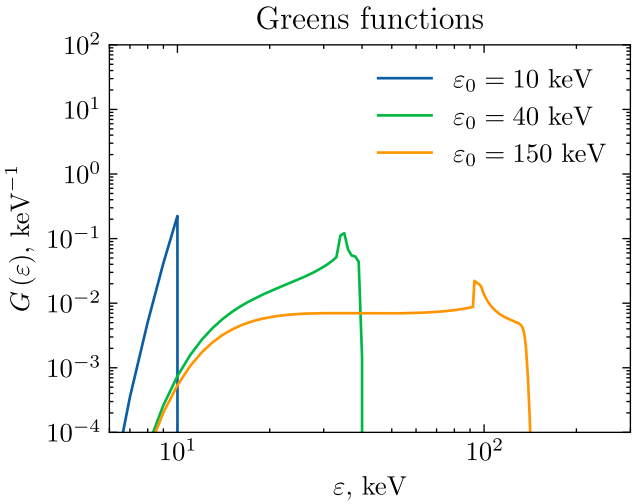


**Figure 1.9** Greens functions values for direction $\mu = 0.7$ and initial photon energies $\varepsilon_0 = 10, 40, 150$ keV.

## 1.4 Radio emission

The second most important emission is on the radio wavelengths.

### 1.4.1 Gyrosynchrotron radiation

This emission is generated by the electrons travelling down to the chromosphere along the field lines. To understand this, let us explore what is going on on the edge of the red and green regions in Figure 1.8.

First, we define our coordinate system. We will operate on such a spatial scale that the field lines going from loop top to the footpoint can be considered homogeneous (at some small region). We further assume that the $z$ axis is parallel to them and that the electron was somehow accelerated and injected into this field with the velocity $\mathbf{v}$. In this field, Lorentz force starts acting on the electron as

$$\mathbf{F} = m\frac{\mathrm{d}\mathbf{v}}{\mathrm{d}t} = q\mathbf{v} \times \mathbf{B}, \tag{1.63}$$

where $m$ and $q$ are mass and charge of the electron. But our field is homogeneous

$$\mathbf{B} = \begin{pmatrix} 0 \\ 0 \\ B \end{pmatrix} \tag{1.64}$$

therefore

$$\dot{v}_x = \frac{qB}{m} v_y \tag{1.65}$$

$$\dot{v}_y = -\frac{qB}{m} v_x \tag{1.66}$$

Now if we multiply 1.66 with imaginary unit $i$ and add both equations together we get

$$\dot{v}_x + i\dot{v}_y = \frac{qB}{m}\left(\dot{v}_x + i\dot{v}_y\right) \tag{1.67}$$

and after substituting $\xi = \dot{v}_x + i\dot{v}_y$ and $\omega_c = \frac{qB}{m}$ we have

$$\dot{\xi} = -i\omega_c \xi \tag{1.68}$$

with the solution

$$\xi = R_L \exp(-i\omega_c t) \tag{1.69}$$

where $R_L$ is the Larmor radius and $\omega_c$ is the cyclotron frequency. So, in words: the electron is gyrating along the $z$-axis (field line). This is the meaning of the spirals on Figure 1.8. And as we know, any acceleration of a charged particle results in electromagnetic radiation, in this case with the frequency $\omega_c$. But the problem is that the electrons accelerated in solar flares are mildly relativistic. Although the motion itself is in principle identical, the directivity of the radiation changes from typical dipole radiation ($\sim \sin^2(\theta)$) to something much more directional, as illustrated in Figure 1.10. This changes the temporal evolution of the field

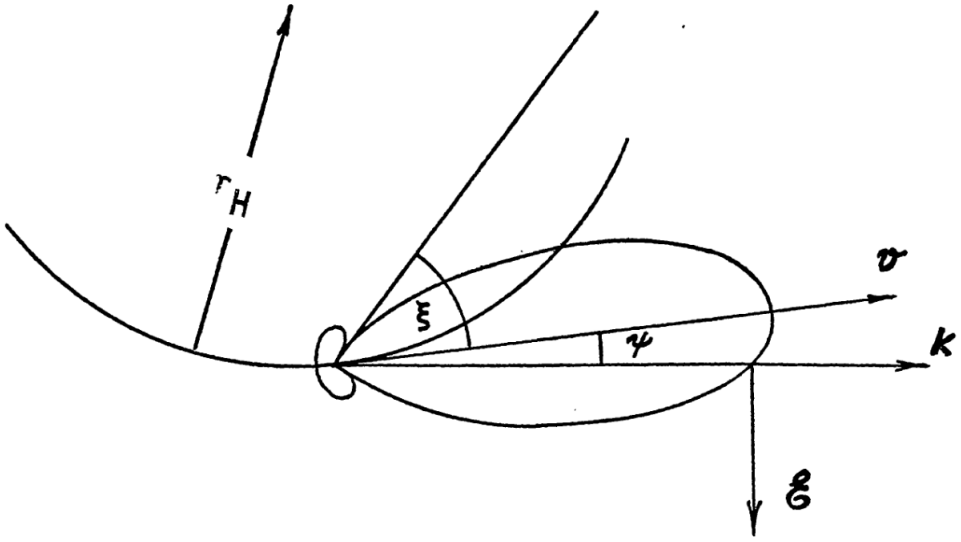


**Figure 1.10** The radiation pattern of a relativistic gyrating particle [15]. As this figure was taken from an article describing this problematic in greater detail, there are some symbols not used in our text. The only relevant symbol is the $r_H$ which is our $R_L$ Larmor radius.

intensity from sin wave to periodical pulses, which is a superposition of more frequencies. This is the difference between nonrelativistic cyclotron and mildly relativistic gyrosynchrotron radiation. We observe emission not at the primary frequency $\omega_c$ but rather on higher harmonics.

This subsection was based on Kulhánek [8].

### 1.4.2 Plasma emission

Now, we will describe the last relevant emission mechanism. We will model plasma as layers of protons and electrons. In rest these layers are perfectly aligned, but it might happen that some external disturbance causes the electron layers to shift infinitesimally by $\xi$ like in Figure For electric field we have

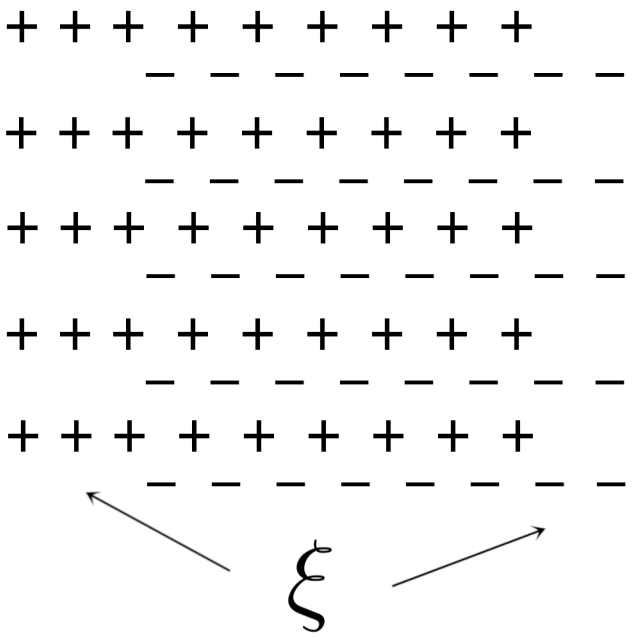


**Figure 1.11** Simple model of oscillating plasma with the properties of a harmonic oscillator: the higher the displacement $\xi$ of electrons is, the stronger force pulls them back.

$$\mathrm{d}E = \frac{ne}{\varepsilon}\mathrm{d}\xi \tag{1.70}$$

where $n$ is the ion density, $e$ is the elementary charge and $\varepsilon$ is the permittivity. The electric intensity acts on the electron with force

$$F = Ee = \frac{ne}{\varepsilon}\xi = -m\frac{\mathrm{d}^2\xi}{\mathrm{d}t^2}, \tag{1.71}$$

where $m$ is the mass of the electron. We can see that such a configuration results in oscillatory motion of the layers with the frequency

$$\omega_p = \sqrt{\frac{ne^2}{m\varepsilon_0}} \tag{1.72}$$

This subsection was inspired by [1] and [8]

## 1.5 Wavelet transform

Another interesting aspect of solar flares are so called Quasi Periodic Pulses (QPP) [16]. Although the exact definition is a bit unclear, by this term we will denote the observation of few periods of oscillation of flux often on different wavelengths. How does one analyse such a behavior? The first instinct would be to use the Fourier analysis but this would not suffice because it would provide us only with information about periods that appeared in the light curve but not about when did it happen. For this we use the wavelet transform.

The general idea of Fourier transform is correct, we need to find out how similar is the light curve with some periodic function at a given period (which we measure with dot product), but we need to localise it not only in period space but also in time. We do it simply by multiplying the complex exponential with a Gaussian. Let us show it on some equations. First let us remind us of a definition of cross-correlation

$$(f \star g)(\tau) = \int_{-\infty}^{\infty} \overline{f(t-\tau)} g(t)\,\mathrm{d}t. \tag{1.73}$$

This simply tells us how similar are functions $f$ and $g$ when $f$ is shifted in time by $\tau$. We want to know how similar is our light curve $F$ to $\exp(i\omega t)$ in time $\tau$ for different $\omega$. But the exponential has the same intensity in the whole domain, so for localisation in time we damp it by a Gaussian

$$(\psi \star F)(\tau) = \int_{-\infty}^{\infty} \overline{\psi(t-\tau)} F(t)\,\mathrm{d}t = \int_{-\infty}^{\infty} \exp\left(-t^2\right) \exp\left(i\omega(t-\tau)\right) F(t)\,\mathrm{d}t. \tag{1.74}$$

This is the essence of wavelet transform, the formal definition from Torrence [17] for discrete sequence $x_n$ (our light curve data) is

$$W_n(s) = \sum_{n'=0}^{N-1} x_{n'} \overline{\psi\left(\frac{(n'-n)\,\delta t}{s}\right)}, \tag{1.75}$$

where $s$ is the wavelet scale (period), $n$ is the time index, $\delta t$ is the time step and $\psi$ is the mother wavelet. In our analysis we used the Morlet mother wavelet exclusively, which is basically scaled Gaussian multiplied by complex exponential as shown on Figure 1.12.

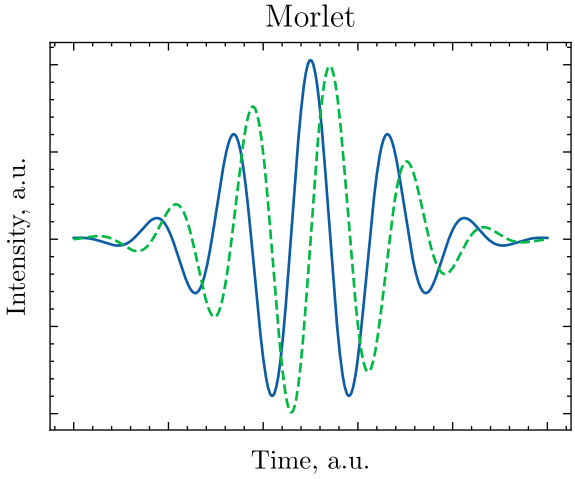


**Figure 1.12** Real (solid) and imaginary (dashed) parts of the Morlet mother wavelet

The scaling is very important because we need to be able to compare the cross-correlations for different frequencies, but the change of frequency causes a change of the norm of a simple mother wavelet we used in equation 1.74 (so strictly speaking it is not a mother wavelet for it must be scaled to be called so).

Now we have the real and the imaginary part of $W_n(s)$. If there is a period in our data, these two are periodical on some $s$ (cross-correlation of two functions

with the same period must be again periodic function with this period, with extrema around $\tau = k\pi$ and zeroes around $\tau = \frac{k}{2}\pi$ for some integer $k$) and with phase shift of $\pi/2$. Now we only have to add their second powers to get rid of the periodicity and negativity

$$P(n,s) = |W_n(s)|^2 . \tag{1.76}$$

And just like that, we obtain the power spectrum, which is exactly what we were looking for.

We have now some information about the quasi-periodicity of our data but how do we tell if it is a true feature or just some noise? First tool to make the result more exact is the cone of influence. It counters the problem with the signal being finite series. So in the beginning and ending times, the mother wavelet might already be partially out of the light curve. Therefore, we will consider only the part of the wavelet spectrum where the most of the mother wavelet is already in the signal time interval ($e$-folding time). But this value changes with periods, as mother wavelet widens. Eventually, the part of wavelet that we are not using creates a shape of a cone hence the name. For Morlet mother wavelet, the cone of influence line is $\sqrt{2}s$

The cone of influence treats problems introduced by the method itself but what if our data contain some random periodicity? There are two main models of a solar noise used in wavelet transform; the white noise and the red noise. They are defined by their Fourier spectra, white noise having constant power on every frequency whereas red noise having power-law power distribution in frequencies. The idea is to compare the noise wavelet power with our data.

We assume that the noise is constant in time so we only need to find its local wavelet spectrum - a cut in some time through the periods. We know how the overall trend should look like (constant or power-law)[4]. Torrence uses this fromula for noise modelling

$$P_k = \frac{1-\alpha^2}{1+\alpha^2-2\alpha\cos 2\pi k/N}, \tag{1.77}$$

where $N$ is the number of frequencies and $k = 0, ..., N/2$ is the frequency index. For $\alpha = 0$ $P_k$ is a constant, for $\alpha \to 1$ $P_k$ is close to a power-law. Since the noise is random variable with normal distribution, its power spectrum will have the distribution of $\chi^2_2$. The 95% confidence contour line is the contour where

$$|W_n(s)|^2 > \frac{1}{2}\sigma^2 P_k \chi^2_2(0.95), \tag{1.78}$$

where $\sigma^2$ is the variance and $|W_n(s)|^2$ is the wavelet power spectrum of our data.

This section was based on [17]

[4]This, however, is the trend in the frequency space, not the period

# 2 Instruments

As we have already seen in the previous chapter, the impulsive phase can be theoretically observed on many different wavelengths. We have not carried out any observations ourselves, but rather used available data from instruments discussed in this chapter.

## 2.1 SOLO

The Solar Orbiter (SOLO) is an ESA-led mission with strong NASA participation. It was designed to address questions such as "How does the Sun create and control the heliosphere - and why does solar activity change in time?" The payload consists of ten experiments. Four of them are sensors for in-situ measurements, the remaining six are for remote imaging of the Sun and its atmosphere [18]. One of them is the Spectrometer/Telescope for Imaging X-rays (STIX) which is the instrument that provides the main body of data for our analysis.

### 2.1.1 STIX

The STIX provides diagnostics of the hottest thermal plasmas in the solar corona and information on nonthermal electrons that are accelerated above 10 keV during solar flares. Schematically, it consists of two main components; the imager and the Detector/Electronics Module (DEM) see Figure 2.1. The imager

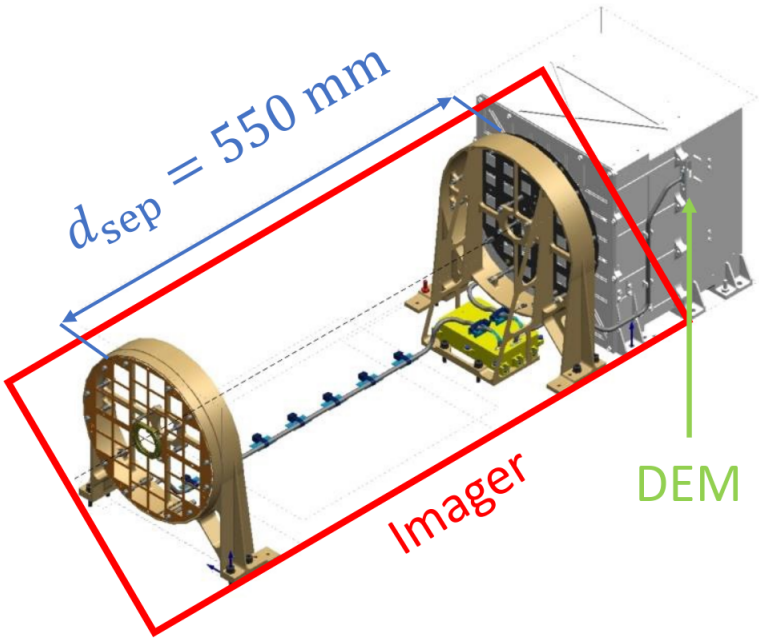


**Figure 2.1** Scheme of STIX [19] with its two main components the imager and the DEM

consists of two arrays of 32 grids, DEM follows with corresponding 32 CdTe X-ray detectors, allowing spectral analysis in the interval between 4-150 keV [20]. The

triads of the corresponding grids and detector are called subcollimators and are numbered in Figure 2.2 Each detector is coarsely pixelated, with four top and

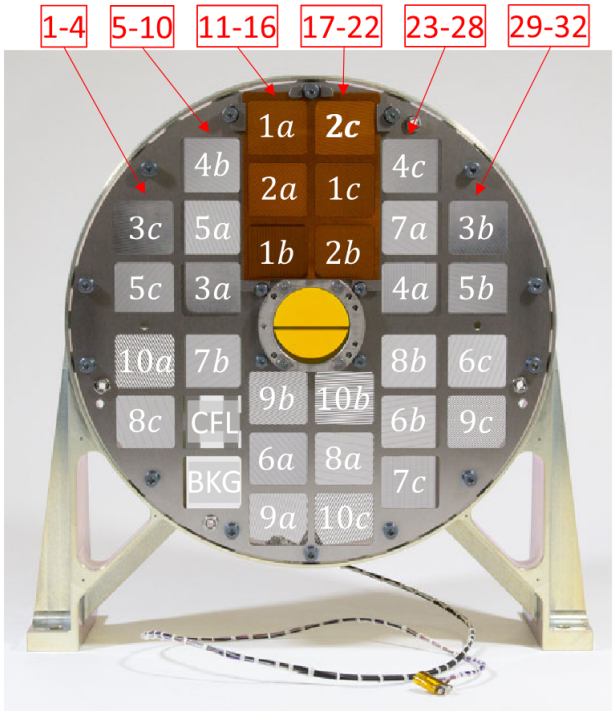


**Figure 2.2** Numbered subcollimators [19]. In lower left can be seen Coarse flare location (CFL) and background (BKG) subcollimators. The upper reddend subcollimators are not used for image reconstruction because they are not properly calibrated

bottom pixels and four smaller central pixels (shown in green in Figure 2.3). The subcollimators labeled as BKG and CFL are not used for spectral analysis. CFL stands for coarse flare location; its rear window is open, while the front window contains six small holes, allowing each potential flare location to cast a unique illumination pattern onto the detector. From these the flare location is estimated. These patterns are then used to estimate the flare's location. In contrast, the BKG subcollimator has an open front window and an almost closed rear window. BKG stands for background because this subcollimator measures the background noise. Both of these subcollimators are illustrated in Figure 2.3 Apart from a natural background, all detectors are artificially illuminated by X-rays from radioactive Ba source for energy calibration.

### Image reconstruction

This subsection is extract from [19]. Besides spectral analysis, STIX is able to approximate the spatial distribution of the X-ray source. To do this, the instrument employs a Fourier transform imaging technique [19]. As we said before, all the windows (all but 9 and 10) have vertical grids. But the grids in the front and rear windows are not the same, instead they are different in pitch (sum of the widths of slit and slat) and/or orientation. This gives rise to Moiré patterns on the detector surface. The period and orientation of such Moiré pattern are given

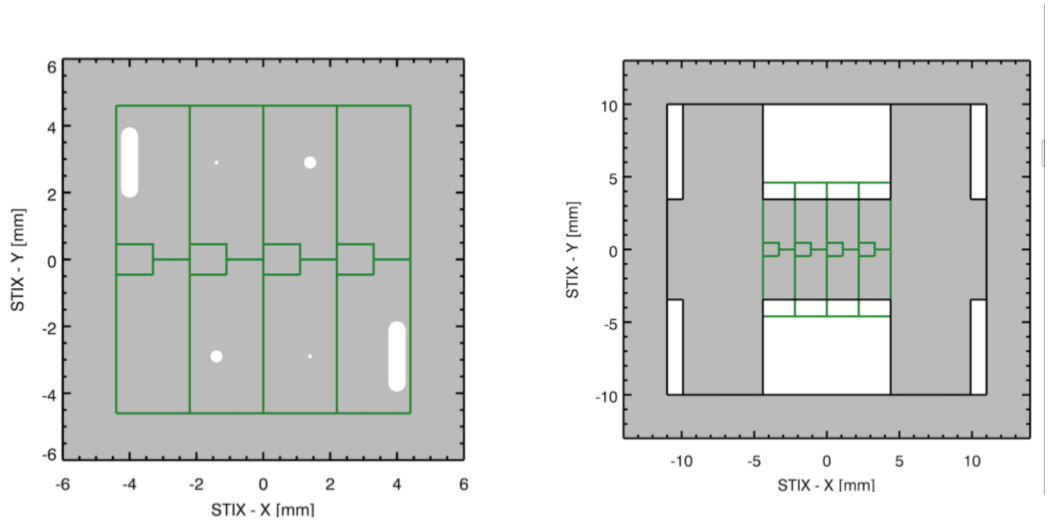


**Figure 2.3** BKG (left) and CFL (right) subcollimators [18]. The green lines designate the projection of the pixels. Since the CFL is on the front part of the imager, the projected pixels appear smaller.

by

$$\mathbf{v} = \frac{1}{p_f}\mathbf{k}_f - \frac{1}{p_r}\mathbf{k}_r, \tag{2.1}$$

where $\mathbf{v}$ is perpendicular to Moiré fringes and its norm is inversely proportional to the period of the pattern, $p$ is the pitch of the grid, $\mathbf{k}$ is a unit vector perpendicular to the slits. Subindeces $f$ and $r$ denote front and rear grid. The grids are designed such that the resulting Moiré fringes are aligned parallel to the vertical edges of the detector and the pitches and orientation angles are chosen to fulfill

$$\begin{pmatrix} \pm 1/W \\ 0 \end{pmatrix} = \frac{1}{p_f}\mathbf{k}_f - \frac{1}{p_r}\mathbf{k}_r. \tag{2.2}$$

where $W$ is the width of the detector. Let us now quantify the relationship of Moiré pattern and the observed source, i.e. $\Phi(x, y)$ the function representing the number of X-ray photons emitted in the energy range $[\varepsilon, \varepsilon + \mathrm{d}\varepsilon]$ per unit of time , energy, and angular area from region centered on $(x, y)$ on the solar disk, which result in the number of detected counts per unit of detector area in the same energy range. We can compute the transmitted photon flux as a function of coordinates on the detector

$$M(w, h) = \int\int \Phi(x, y)\, T(w, h; x, y)\, \mathrm{d}x\mathrm{d}y, \tag{2.3}$$

where $T(w, h; x, y)$ is the probability that a photon emitted from $(x, y)$ on solar disk results in count on $(w, h)$ on the detector. This function can be approximated as

$$T(w, h; x, y) \approx \frac{s_f s_r}{p_f p_r} + \sigma \cos\left(\frac{2\pi w}{W} + 2\pi(xu + yv) - \Delta\varphi\right), \tag{2.4}$$

where $s$ is the width of slit, $\varphi$ is the window phase difference and

$$\sigma = \frac{2}{\pi^2} \sin\left(\frac{\pi s_f}{p_f}\right) \sin\left(\frac{\pi s_r}{p_r}\right). \tag{2.5}$$

Now we can calculate the photon flux

$$M(w,h) = F\frac{s_f s_r}{p_f p_r} + \sigma \int\int \Phi(x,y)\cos(2\pi(xu+yv)-\gamma)\,\mathrm{d}x\mathrm{d}y, \tag{2.6}$$

where

$$\gamma = \frac{2\pi w}{W} - \Delta\varphi \tag{2.7}$$

makes our life easier and

$$F = \int\int \Phi(x,y)\,\mathrm{d}x\mathrm{d}y \tag{2.8}$$

is the total flux emitted. Let us now define visibility as a Fourier component and Fourier transformation of $\Phi$

$$\begin{aligned} V(u,v) &= \mathcal{A}(u,v)\exp(i\omega(u,v)) = \\ &= \int\int \Phi(x,y)\exp(2\pi i(xu+yv))\,\mathrm{d}x\mathrm{d}y. \end{aligned} \tag{2.9}$$

so the flux is

$$\begin{aligned} M(w,h) &= F\frac{s_f s_r}{p_f p_r} + \mathrm{Re}\left(\exp(i\gamma)\,\sigma\int\int \Phi(x,y)\exp(2\pi(xu+yv))\,\mathrm{d}x\mathrm{d}y\right) = \\ &= F\frac{s_f s_r}{p_f p_r} + \sigma\mathrm{Re}(\exp(i\gamma)\,V(u,v)) = \\ &= F\frac{s_f s_r}{p_f p_r} + \sigma\mathcal{A}\cos(\omega+\gamma). \end{aligned} \tag{2.10}$$

We can express the number of counts in each vertical stripe as

$$\begin{aligned} A &= \mathcal{P}\left(F + \mathcal{E}\mathcal{A}\cos\left(\frac{3\pi}{4}+\omega-\Delta\varphi\right)\right), \\ B &= \mathcal{P}\left(F + \mathcal{E}\mathcal{A}\cos\left(\frac{\pi}{4}+\omega-\Delta\varphi\right)\right), \\ C &= \mathcal{P}\left(F + \mathcal{E}\mathcal{A}\cos\left(-\frac{\pi}{4}+\omega-\Delta\varphi\right)\right), \\ D &= \mathcal{P}\left(F + \mathcal{E}\mathcal{A}\cos\left(-\frac{3\pi}{4}+\omega-\Delta\varphi\right)\right), \end{aligned} \tag{2.11}$$

where

$$\mathcal{P} = \frac{WH}{4}\frac{s_f s_r}{p_f p_r}, \quad \mathcal{E} = \frac{2\sqrt{2}}{\pi}\frac{p_f p_r}{s_f s_r}\sigma. \tag{2.12}$$

Finally we can calculate

$$\mathcal{A} = \frac{1}{2\mathcal{P}\mathcal{E}}\sqrt{(C-A)^2 + (D-B)^2} \tag{2.13}$$

and

$$\omega = \mathrm{atan2}(D-B, C-A) + \frac{\pi}{4} + \Delta\varphi, \tag{2.14}$$

where $\mathrm{atan2}(b,a)$ denotes the angle in polar coordinates corresponding to vector $(a,b)$; the angle $a$ is measured counter-clockwise from the positive $a$ axis. From these equations we can compute the visibility

$$V(u,v) = \mathcal{A}\exp(i\omega), \tag{2.15}$$

and execute the source reconstruction at last. Let us now explore the ways of realization of this process.

### Back projection

We are able to compute the Fourier transform of the source (2.9), but this equation does not give us complete transformed image, visibility is only one point the frequency domain. We have 32 subcollimators, 2 of them are not used for this measurement and because

$$V\left(-u,-v\right)=\overline{V\left(u,v\right)}, \tag{2.16}$$

we get 60 point in the frequency domain. The first, simplest and perhaps most

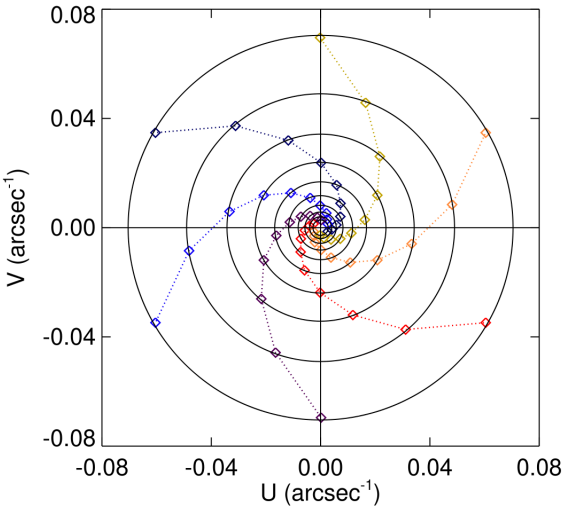


**Figure 2.4** Frequencies sampled by the STIX sub-collimators. As a reference, the ten circles on which the frequencies lie are plotted in black. [18]

inaccurate method is straightforward inverse discrete Fourier transform of those 60 points.

### CLEAN

The problem of back projection is that in reality, the inverse transform does not result in the source image but rather in a convolution of it and the PSF of STIX, also known in radioastronomy as a dirty map [21]. The CLEAN algorithm addresses this problem by iteratively subtracting the dirty beam (see Figure 2.5). It finds the brightest pixel on the dirty map, places it in the clean map, and subtracts the dirty beam from the dirty map. It repeats these steps until the dirty map is only noise. This method is on one hand quite efficient, on the other it can introduce artifacts to the reconstructed image.

We also used MEM GE method described in A.1 but only to check on CLEAN and we do not present any results achieved by this method.

## 2.2 SDO

The Solar Dynamics Observatory (SDO) is a NASA Earth-orbiting satellite launched in 2010. It is designed to provide the data and scientific understanding necessary to predict solar activity. It is doing so using three scientific instruments:

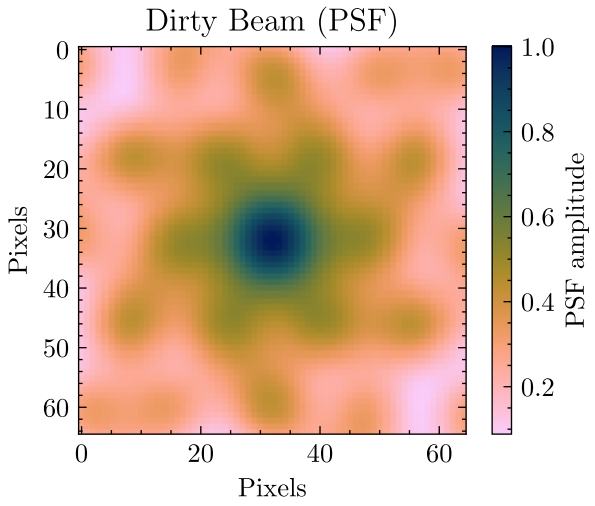


**Figure 2.5** Dirty beam used by the CLEAN algorithm

Atmospheric Imaging Assembly (AIA), EVE and HMI [22]. We will only use the data from AIA.

### 2.2.1 AIA

AIA is an array of four telescopes that observes the surface and atmosphere of the Sun. These telescopes combined with narrow-band filters can observe in 10 different channels (wavelengths) [23]

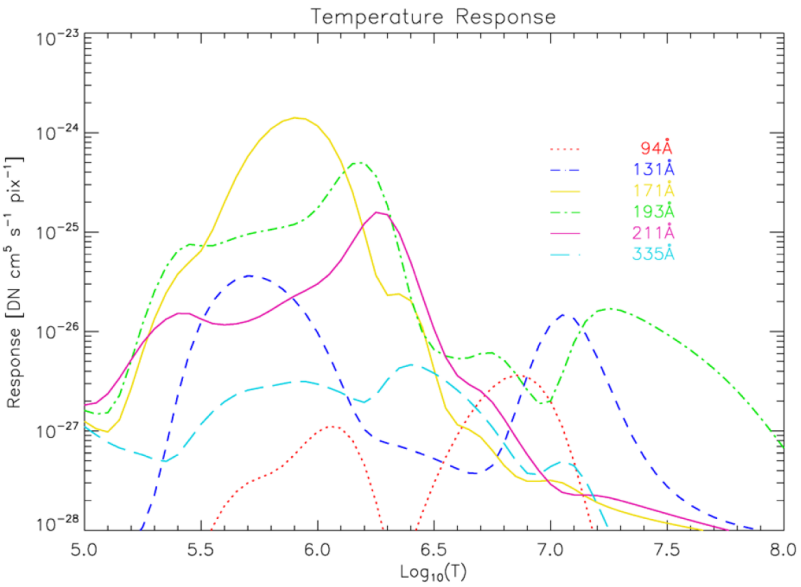


**Figure 2.6** The response functions of EUV filters [24]. Note that the response is a function of $\log T$ similarly to Figure 1.1; this is why some physical region could be assinged to the filters.

EUV channels [23] [25]:

- 94 Å, Fe XVIII line, flaring regions

- 131 Å, Fe VIII, XXI lines, flaring regions
- 171 Å, Fe IX line, quiet corona, upper transition region
- 193 Å, Fe XII, XXIV lines, corona and hot flare plasma
- 211 Å, Fe XIV line, active region corona
- 304 Å, He II line, chromosphere, transition region
- 335 Å, Fe XVI line, active region corona

UV channels [23] [25]:

- 1600 Å, C IV line, transition region, upper photosphere
- 1700 Å, C IV nearby continuum, temperature minimum, photospehere

Visible channel [23] [25]:

- 4500 Å, white light continuum, photosphere

The filter response as a function of temperature is shown in Figure 2.6 (only for 6 EUV filters)

## 2.3 Radiotelescopes

### 2.3.1 Ondřejov

The Ondřejov solar radiotelescopes are located at the Astronomical Institute of the Czech Academy of Sciences in Ondřejov. Our data were obtained from the 10-meter dish antenna RT5, which operates in the 800–2000 MHz range with a temporal resolution of 0.1 s.[1].

### 2.3.2 Learmonth

We also used data from Learmonth solar observatory in Australia which is a part of the Radio Solar Telescope Network (RSTN) with other observatories at Massachusetts, Hawaii, New Mexico and Italy. Although our primary dataset came from Learmonth, we verified its consistency with data from the San Vito observatory in Italy. Learmonth is jointly operated by the Australian Bureau of Meteorology – Australian Space Weather Forecasting Centre and the U.S. Air Force. Three dish antennas monitor eight frequency bands: the 8.5 m dish observes at 245, 410, and 610 MHz; the 2.4 m dish covers 1415, 2695, 4995, and 8800 MHz; and a 1 m dish monitors 15400 MHz.[2]. The data have 1 s temporal resolution and are available here: `https://www.sws.bom.gov.au/World_Data_Centre/1/10`

[1] More information: `https://www.asu.cas.cz/~radio/`

[2] More information about the observatory: `https://www.sws.bom.gov.au/World_Data_Centre/3/1/46?utm_source=chatgpt.com`

# 3 Data analysis

The subject of our analysis will be the solar flare from 2021-10-09 that took place in Active Region (AR) 12882. This event marked the highest X-ray flux recorded for this active region in its observational history[1]. For quick assessment of the magnitude of the flare, the GOES classification is widely used in the solar flare physics community. For this classification, refer to Table 3.1[2].

| Class | Peak Flux ($\mathrm{W\,m^{-2}}$), 1–8 Å |
|---|---|
| B$k$ | $k10^{-7}$ |
| C$k$ | $k10^{-6}$ |
| M$k$ | $k10^{-5}$ |
| X$k$ | $k10^{-4}$ |

**Table 3.1** GOES X-ray flare classification based on peak flux in the 1–8 Å band. For classes A through M, the scaling factor $k$ satisfies $0 < k < 10$. However, this constraint does not necessarily apply to X-class flares.

The flare was classified as a GOES M1.6 event. At the time of the flare, SOLO was relatively close to Earth, so both STIX and AIA observed the flare on the solar disk from similar perspectives. However, since SOLO was slightly closer to the Sun, we had to apply a time shift of 159 s to all STIX observation times. This time difference accounts for the varying light travel times between SOLO and Earth, called the light correction. The spatial configuration of SOLO, Sun, and Earth is illustrated in Figure **??**.

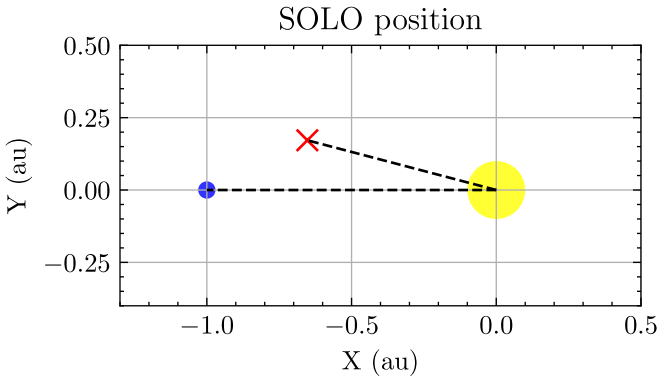


**Figure 3.1** Configuration of SOLO, Earth and Sun during the flare projected to the ecliptic plane. The angle SOLO-Sun-Earth was around 15 deg, distance of SOLO from Sun was 0.68 AU.

This flare was chosen for the potential interesting interplay of HXR and radio fluxes. In Figure 3.2 the time profile of the X-ray emission can be seen, with the growing (impulsive) phase at the beginning and later decaying phase. We wanted to go deeper in studying the beginning of the impulsive phase where the radio

[1]History of the AR available here `http://helio.mssl.ucl.ac.uk/helio-vo/solar_activity/arstats/arstats_page5.php?region=12882`

[2]More information available at `https://hdrl.gsfc.nasa.gov/LWS_Space_Weather/GOES_Xray_descrip.html`

emission on 1 GHz is also prominent, i.e. around 06:28:30-06:32:30, rather than covering the whole phase with less detail.

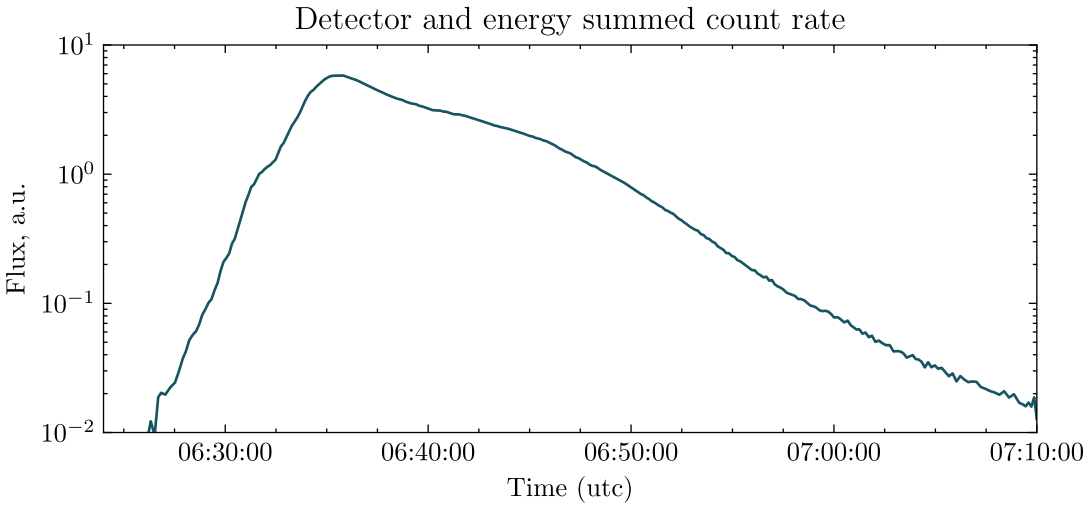


**Figure 3.2** Count rate summed for all energies (4-150 keV).

This specific event was previously studied. In the article *The existence of hot X-ray onsets in solar flares* [26] this flare is one of four studied cases of the onset phase, which refers to the early X-ray emission before the sudden increase in nonthermal emission during the impulsive phase. Thus, a different time interval was studied, with different objectives.

In the article *Multiple injections of energetic electrons associated with the flareCoronal Mass Ejection (CME) event on 9 October 2021* [27] the impulsive phase was analysed in HXR and radio band. However, the aim of this study was to identify the sources of Solar Energetic Particles (SEP)s. Their analysis covers a broader time range, extending from 06:19 to as late as 08:00, providing a broader picture.

Another mention of this flare is in the article *The observational evidence that all microflares that accelerate electrons to high energies are rooted in sunspots* [28]. In this work, few events from AR 12882 are compared, with the primary focus, however on microflares.

A more thorough discussion of these works with our results will be presented in section 3.4.

## 3.1 Spectral analysis

For our analysis, we used Object Spectral Executive (OSPEX), an object-oriented interface for X-ray spectral analysis of solar data in Interactive Data Language (IDL). However, before using OSPEX, we need to make some modifications to the input files. Fortunately, these modifications are known and designed by the STIX team.

We downloaded the data in FITS format from the Solar Orbiter STIX Data Center[3], which included one file for background subtraction (unique ID: 2110090101)

[3]Available here: `https://datacenter.stix.i4ds.net/view/list/bsd`

and one for the analysis itself (unique ID: 2110090002). First, we needed to extract the metadata. This involved finding the Energy Lookup Table (ELUT) that was applied in-flight during the observation. We also had to store the values for the distance to the Sun and the light-time correction. Once this was done, we specified the spex file reader and the files were ready to be analyzed directly in OSPEX, where background subtraction took place. There are two main methods for accounting for background. First does not require any special file and works simply by fitting the non-solar signal level from the beginning or the end of the flare. The second one needs BKG file containing quiet-Sun count rate from before the flare as input. We used the second method. As we have shown in the section 1.3 we expected that the spectrum will contain thermal part 1.38:

$$I(\varepsilon) = k_1 \overline{Z^2} \frac{Q}{\varepsilon T^2} \exp\left(-\frac{\varepsilon}{k_B T}\right), \tag{3.1}$$

where $k_1$ is according constant scaled, however, by the distance from the Sun. Therefore the units of $I$ are $\mathrm{s}^{-1}\ \mathrm{J}^{-1}\ \mathrm{m}^{-2}$. This part is fitted with a function called Variable Thermal (vth) with following parameters

$$\text{vth} \begin{cases} \text{emission measure } Q \\ \text{plasma temperature } T \\ \text{relative abundance } \overline{Z^2} \text{ (fixed)} \end{cases}$$

The relative abundance was considered to be a constant throughout the flare, therefore, it is the only fixed parameter. The spectrum should also contain nonthermal part 1.43

$$I(\varepsilon) = k_2 \int_{\varepsilon}^{\infty} F(E_0, N, \delta_L, \delta_H, E_B, E_L, E_H) \int_{\varepsilon}^{E_0} \frac{\sigma_B(\varepsilon, E)}{\sigma_C(E)} \frac{\mathrm{d}E}{E} \mathrm{d}E_0 \tag{3.2}$$

where $k_2$ is according constant scaled by the square of distance as well resulting in the same units of $\mathrm{s}^{-1}\ \mathrm{J}^{-1}\ \mathrm{m}^{-2}$. We have shown more specific form for a single power-law electron distribution in equation 1.54, but as we will see, we will eventually fit the broken power-law more, thus the general form. This part is fitted with a function called thick2 (named after the thick target model, see Subsection 1.3.2), which is a time-optimized version of the standard fitting function.

$$\text{thick2} \begin{cases} \text{total integrated electron flux } N \\ \text{low delta } \delta_L \\ \text{break energy } E_B \\ \text{high delta } \delta_H \\ \text{low energy cutoff } E_L \\ \text{high energy cutoff (fixed) } E_H \end{cases}$$

The option to choose broken or simple power-law is implemented by simply fixing the break energy at some very high number (1500 keV was used) and fixing the high delta (i.e. for choosing simple power-law). One function is not mentioned here; the albedo. The albedo will not be fitted but rather looked up from prepared tables as we explained in Subsection 1.3.3.

## 3.2 Image reconstruction

Second part of the analysis of the X-ray data is image reconstruction and reprojection on EUV images, connecting the observations. We use the methods described in 2.1.1. This can always be done only after proper spectrum analysis, as it is essential to determine the appropriate energies to fit for each time interval. The problem is that the shorter the subinterval, the fewer photons we capture. Based on a recommendation of the STIX team, we initially choose to strive to reconstruct images only based on 5000 counts or more. For the thermal part, this is not a problem as the emission is much stronger than nonthermal.

Although many scientists still use IDL for image reprojection, we chose the recently emerging python library stixpy[4]. This led to some confusion in the beginning, for example about the orientation of the reprojected data, but eventually we figured everything out.

In most cases we used the CLEAN algorithm, not only because it is faster than MEM GE, but also does not come with the possible hyper resolution effects and in our opinion is conceptually simpler, more straightforward and therefore easier to grasp and use. However, we still double-checked our CLEAN results with MEM GE.

For downloading and plotting AIA images, we used the aiapy and SunPy python libraries [29] [30]. Initially, we reprojected AIA images onto HXR data, as we used only the 160 nm filter, which mainly shows the photosphere. Because of that, we did not need to worry much about the geometry when aligning the images. However, when we started using data from the 13.1 nm AIA filter, things became more complicated, as this filters response function (see Figure 2.6) makes it sensitive to plasma located higher in the corona (see Figure 1.1 for corresponding heights above the limb), thus making reprojection potentially problematic. From there on, we were reprojecting STIX data to EUV. Not only is it faster, it also does not affect the resolution of the AIA images, as was the prior case. We can do that because the thermal X-ray source should not be that high above the limb and the nonthermal sources are directly in the photosphere. Even if the height of the thermal source was high, the perspective difference of SOLO and SDO is not so large (this is demonstrated in Figure 3.1) and therefore the projection effects are negligible.

## 3.3 Work flow

Now that we have established the theory, instrumentation and implementation, we can finally get to the analysis itself.

### 3.3.1 Fitting spectra and constructing images

After completing the analysis software, we were keen to apply it. Our method of work was essentially trial and error. First we fitted only vth and thick2 but the nonthermal part was not really working (large residuals with clear trend), so we added an albedo correction. From a physical point of view, this is quite

[4]The Git repository is available at `https://github.com/TCDSolar/stixpy`

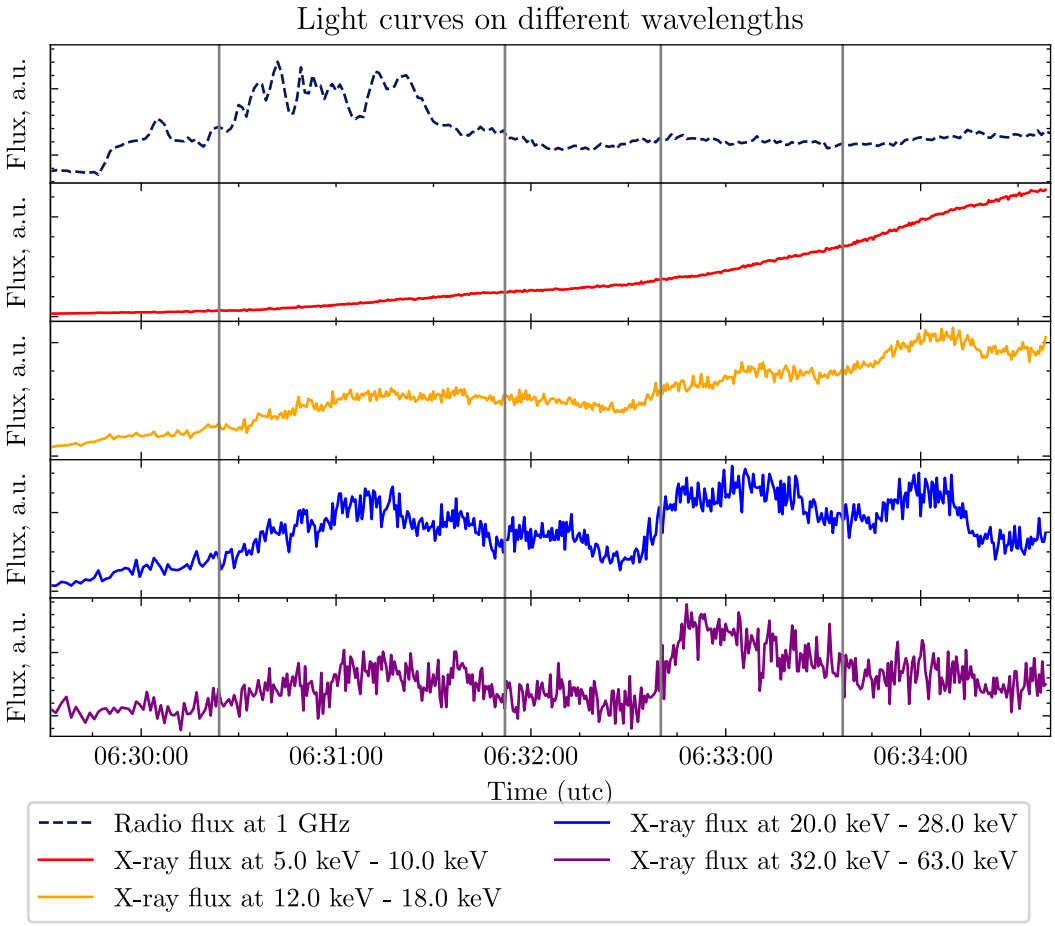


**Figure 3.3** Light curves on different wavelengths in imaging subintervals

reasonable since the flare is near the center of the disk. In the broader analysis of Jebaraj et al. [27], this step was not carried out.

The new spectra gave us the first insight into the temporal evolution of the flare in our time interval. With this knowledge, we determined the temporal and energetical subintervals in which image reconstruction was carried out with only two energetic subintervals (SXR and HXR). From reconstructed and reprojected images we got the spatial-temporal evolution. With these new informations and the wavelet spectra, we decided to shift our interval of interest; there was not much activity in the beginning and on the other hand, there was a interesting peak at around in the end. The new interval was therefore decided to span from 06:29:30 to 06:34:00 containing two main peaks at 06:31:10 and 06:33:00. This is the first and third interval in Figure 3.3.

We proceeded by determining new subintervals in 6:29:30-6:34:00 such that there are at least 5000 counts in the nonthermal energy interval. This was very laborious since we needed precise energy intervals from the spectra to calculate counts and find time intervals yet for the spectra we needed the time intervals. The energy subintervals (SXR HXR) were decided based on spectra; the upper limit of HXR was where the data were getting too noisy, the lower limit was around the energy where fitted nonthermal function was at least ten times stronger than the thermal. The limits of SXR were 4 keV and 12 keV.

We generated new images for these intervals and observed that during the

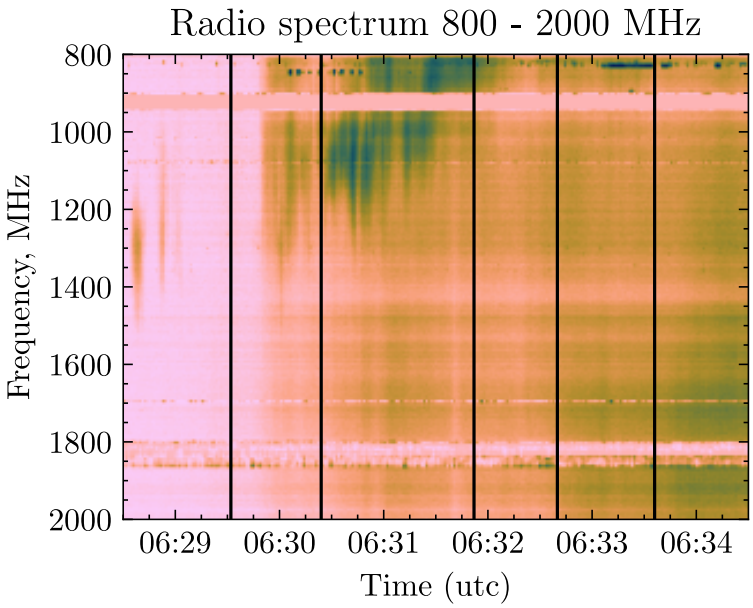


**Figure 3.4** Radio spectrum from Ondřejov radiotelescope RT5. There are some spikes at the beginning around 1300 MHz. This was the reason why we initially wanted to do the analysis from 06:28:30. Eventually, we decided not to do that, shifting the beginning to 06:29:30. The vertical lines designate the subintervals chosen for image reconstruction.

second flux maximum (i.e. at 06:33:00 UT), the HXR emission originated from a different location than in the first (06:31:10). This led us to define new time and energy subintervals. The second HXR source appeared significantly harder (with a lower $\delta$, resulting in a flatter spectrum), so we divided the HXR range into two subintervals: 20–28 keV and 32–63 keV. For SXR, we defined the subintervals as 5–10 keV and 12–18 keV. The latter is likely a mix of thermal and nonthermal emission. We raised the lower limit because the 4 keV energy bin is on the edge of STIX detection ability. Fixing energies like this made it easier to find new time intervals, but they needed to be much longer, and it is still not optimal as could be seen in Table 3.2 (in terms of counts used for reconstruction; we settled for around 3000 counts).

| **Time Range** | **12-18 keV, cts** | **20-28 keV, cts** | **32-63 keV, cts** |
|---|---|---|---|
| 29:32–30:24 | 5 806 | 1 984 | 536 |
| 30:24–31:52 | 30 000 | 11 000 | 3 007 |
| 31:52–32:40 | 31 000 | 5 401 | 1 061 |
| 32:40–33:36 | 45 000 | 10 000 | 4 539 |
| 33:36–34:40 | 70 000 | 8 963 | 2 865 |

**Table 3.2** Intervals accounting for temporal structure of the flare and their numbers of counts in the harder energy subintervals. Higher numbers were rounded. The exact value was not important, rather the fact that they are above 5000 counts.

These new intervals nicely correspond to the temporal evolution of the flare as can be seen in Figures 3.3 and 3.4.

New images confirmed that the second source is indeed much harder (has

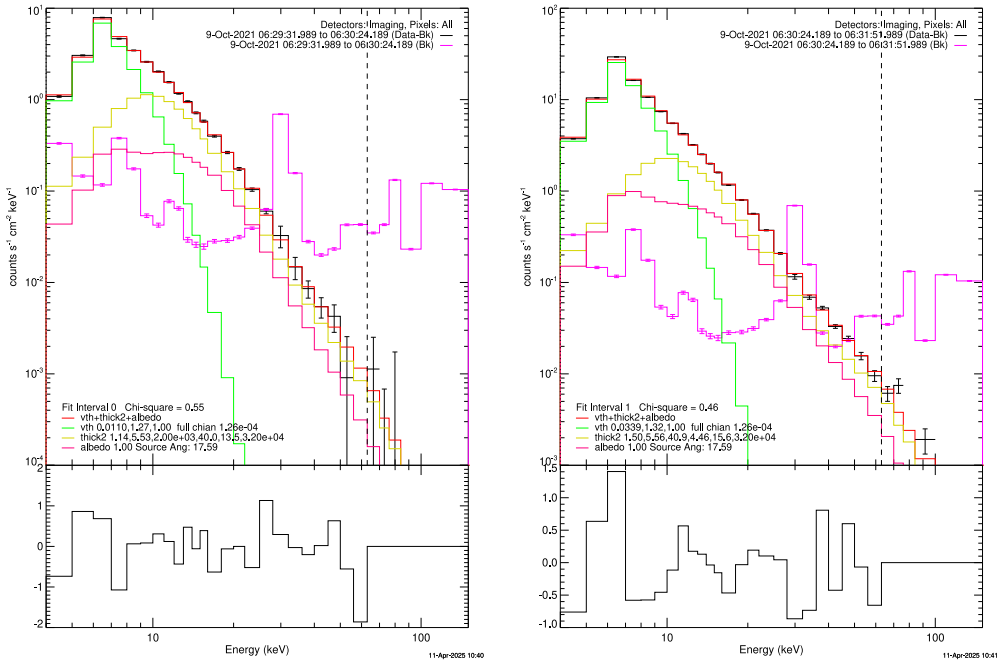


**Figure 3.5** Spectra of the first two subintervals. The lines denote vth (green), thick2 (yellow), albedo (pink), noise (purple) and the fitted spectrum (red). The measured spectrum is black. The dashed line is at 63 keV wich is the edge of fitted energy interval. The first subinterval is the only fitted with simple power-law rather than broken.

flatter electron distribution, lower delta) and explained why the nonthermal fit was still not optimal. Now we fitted these subintervals with broken power-law instead of a simple one, which is explained by merging two different electron distributions. What is very interesting is that the high delta was actually lower than low delta $\delta_H < \delta_L$, i.e. the spectrum is harder on higher energies (see 3.22). It is consistent with the images though, namely with the one from 06:33 (Figure 3.11)with the hard source near the sunspot. The final fits are in Figures 3.5, 3.6, 3.7, the final images are in Figures 3.8, 3.9, 3.10, 3.11, 3.12.

### 3.3.2 Wavelet analysis

As the basis for our wavelet analysis software, we used the Python implementation provided by Torrence [17]. As mentioned earlier, one of the reasons for choosing this particular flare was the radio spectrum in early times, namely 1000 MHz at around 29:50:00-32:00 UT. This emission can be seen in Figure 3.4 and was the first we tried the wavelet analysis on. For this and all subsequent cases, we modeled the noise as a white noise — a choice discussed at the end of this subsection. The wavelet analysis result is presented in Figure 3.13. Due to the power spectrum intensity above the noise, there is probably some QPP, with a period slightly below 40 s and three main peaks around 06:30:00, 06:30:45, and 06:31:15 UT. Additionally, weaker periodicities, such as one near 10 s, appear to fragment the second main peak. Apart from these features, the analysis shows

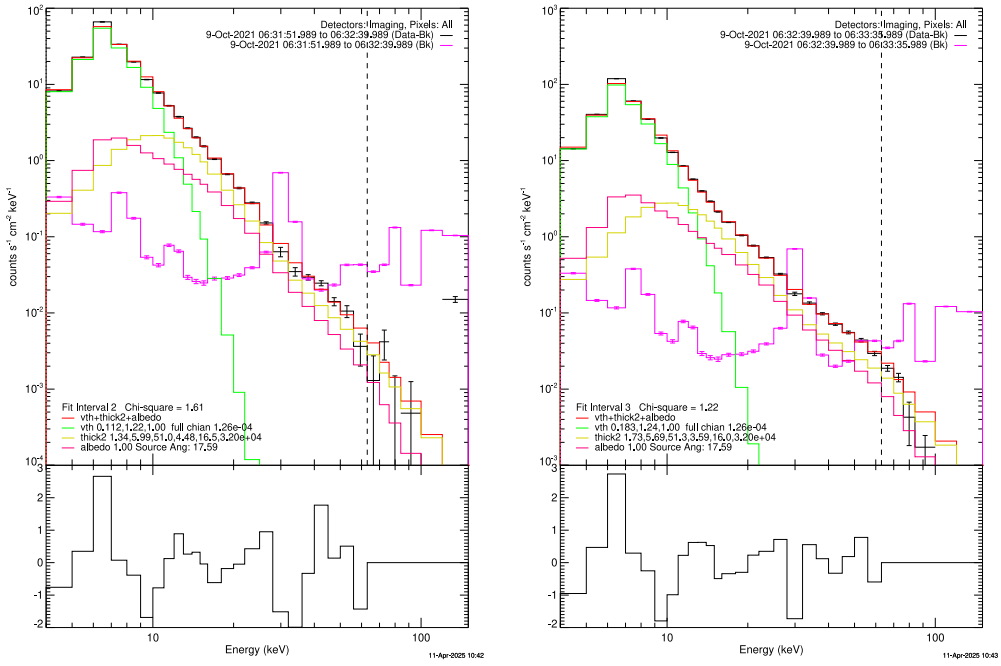


**Figure 3.6** Spectra of subintervals number 3 and 4. There is now clear trend in the residua, at least in the thermal part.

no significant signal beyond the noise level during the selected time interval, as illustrated in Figure 3.4.

Then we performed the wavelet transform on the bulk of our analysis, the HXR data, resulting in Figure 3.14. The nature of wavelet analysis as described in Section 1.5 requires the signal to have the same time step throughout the time interval. This was fullfiled by the radio data however, the time step does change in time for the HXR data. To address this, we created a Python script to downsample the data to match the largest time step in the series. However, the early portion of the HXR data featured time steps roughly three times longer than the rest. Since this initial segment was not that important for our analysis, we dumped the first 40 data points, improving the time resolution from 3 to 1.2 s. Again, due to the wavelet power, there seems to be a QPP on a similar frequency but at a different time. Also, there are no shorter quasi-periods this time. This overall discrepancy could be interpreted by identifying the 1000 MHz emission with type III radio emission (for classification of solar radio bursts refer to [7]). This would mean that there is some hot plasmoid drifting higher above the solar surface, thus changing its density and plasma frequency. But analysing lower frequencies was complicated. Ondřejov provided no data in the lower frequency bands due to high interference, and the RSTN data were inconsistent as the light curves from San Vito and Learmonth differed noticeably. Still, neither dataset showed any evidence of a QPP around 35 s.

Puzzled with uncompatible results, we tried analysing higher frequencies instead. This is visualized in Figure 3.15. If we compare it to 3.14 we immediately see similarities in the light curve and understandably in the wavelet power spectrum

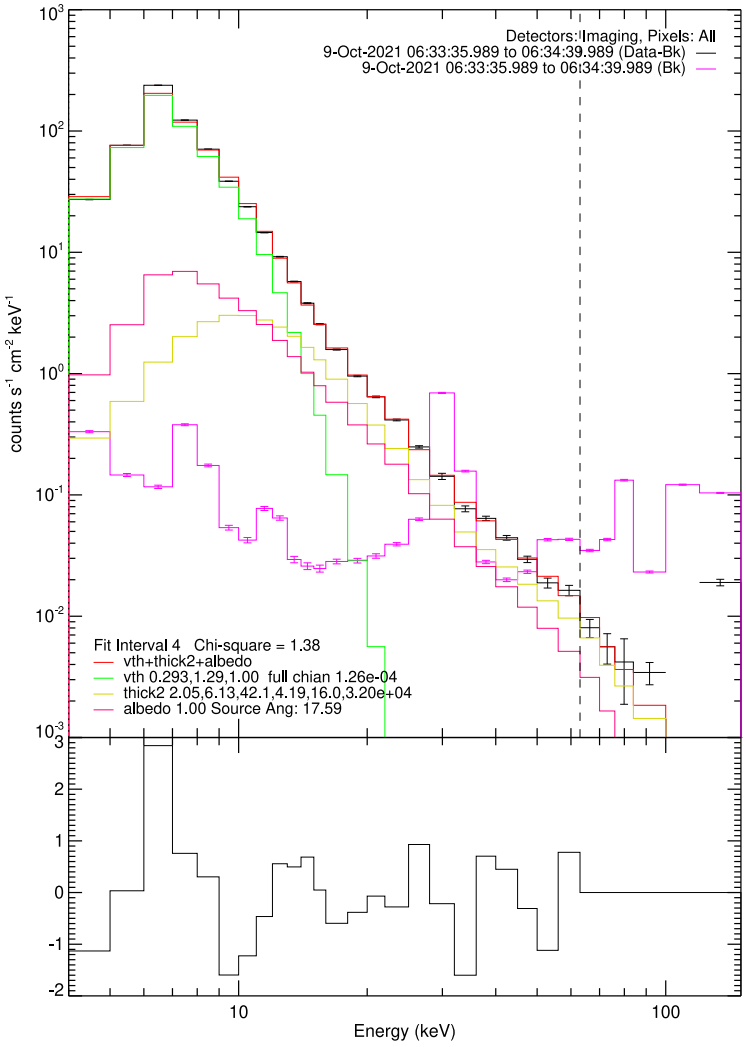


**Figure 3.7** Spectrum of th last subinterval.

as well, namely the weaker peak around 06:31:10 followed by a strong peak at around 06:33:00. There might be some periodicity, but this time, the power is much stronger on longer periods near the 06:33:00. These similarities are illustrated in Figure 3.16, which shows the rebinned and trimmed power spectra used for the cross-wavelet analysis, along with the crosswavelet itself..

But if we stop for a moment and think about it, we discover one small detail; the strongest period of 4995 MHz flux is longer than 60 s but only on the interval of size of 100 s, meaning that there is maybe two but more likely one period. But this is not anything new since from our spectral and imaging analysis we know that there are two main peaks in the flux. It seems like this broader trend is overshadowing what we are looking for in shorter periods.

An approach to address this is to analyze the data after removing the longer-term trend, a process known as detrending. This method, however, lies at the

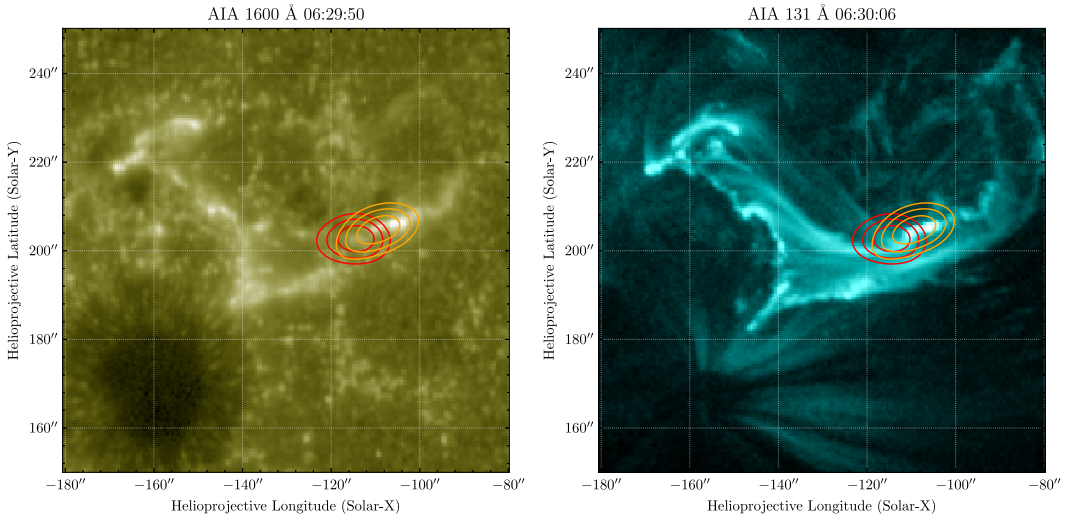


**Figure 3.8** Image reconstruction of the first subinterval. Contours are on 70 %, 80 % and 90 % of 5-10 keV (red) and 12-18 keV (orange). The northern emission from the onset of the flare is already being overshined by the western region. The HXR emission is still weak.

boundary of acceptable data analysis practices, and its use will be discussed later on. Description of our implementation of the detrending method is in the appendix A.2.

For the detrended light curves refer to Figure 3.17. For better orientation, lines designating our five time intervals were added. This figure also justifies their choice for in the first interval we do not see any prominent peak of a pertinent QPP (but this might be caused by the trim required by the resampling), whereas in the second interval there are three of them. In the third one, there is an overall decline of the intensity followed by the total maximum in the fourth. There is another peak in the fifth interval which does not seem to be a continuation of the QPP. The corresponding wavelets and crosswavelet are shown on the Figure 3.18. This time it is clear that there is some QPP with period below 40 s. What is less clear is why is the power intensity shifted in time so much compared to 1 GHz wavelet (see 3.13). The explanation of this problem is quite prosaic; we only need to recontemplate what wavelet transform actually is, namely that the first idea was that we will measure correlation of our signal and the mother wavelet. However, the strength of this correlation is caused not only by the signal shape (period) but also its intensity (amplitude). Let us now illustrate this fact on a signal modeled to the likeness of the detrended light curve in Figure 3.17. If we use wavelet analysis on a signal with constant period but different amplitude of the last pulse the wavelet power will be according so. Figure 3.19 demonstrates this clearly. Now we know, why the wavelet power is shifted in time and we can declare it an artifact. Although the first peak of 1 GHz is shifted, the second corresponds with 5 GHz and HXR nicely. The quasi-period should be around 37 s.

We also tried to perform the wavelet transform on mean AIA pixel values of different regions in different time. Figure 3.21 illustrates this, namely the mean value in a region near the sunspot in the whole time interval (06:29:30-06:34:40). There are hints of similarities, for example the great dimming before 06:33, or

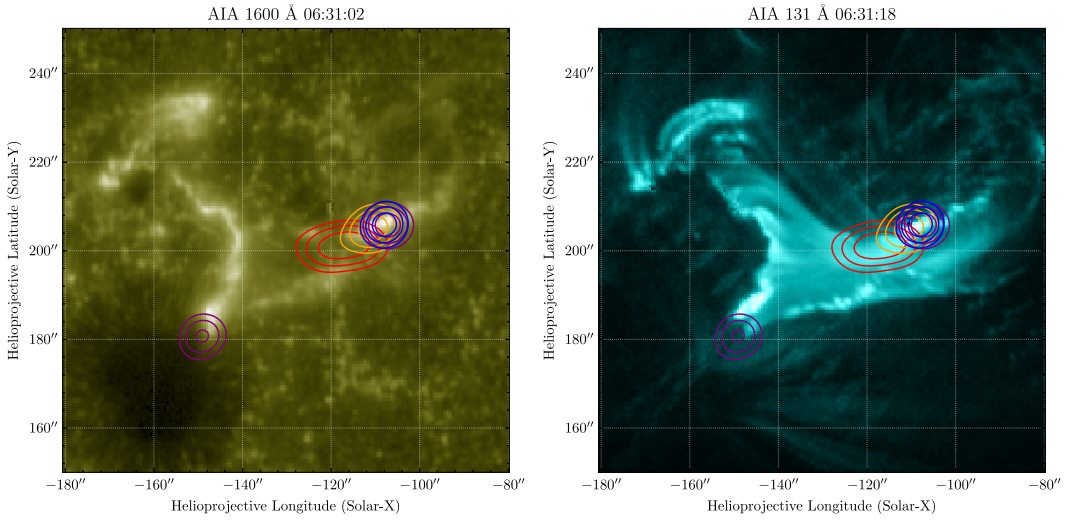


**Figure 3.9** Image reconstruction of the second subinterval. Contours are on 70 %, 80 % and 90 % of 5-10 keV (red), 12-18 keV (orange), 20-28 keV (blue) and 32-63 (violet). The northehrn emission from the onset of the flare is already being overshined by the western region. The HXR emission is still weak.

potential periodicity in the second interval, but the time resolution is too low (12 s) for any meaningful results. This is interesting because if we take the mean pixel values off of the whole AR and not only the close surrounding of the sunspot, the light curve is much more similar to SXR, as could be seen in Figure 3.20

For the confidence contour, we need to model the background noise. We assumed that the background during the flare is the same as on the quiet Sun, which should be white noise. This was recommended to us in private communication but there are some published works that use this method [31]. The problem is that according to Inglis [32], the noise during a solar flare is actually red, i.e. it has a power-law spectrum. This would not only make our confidence interval smaller but the detrending method would be principally wrong since by filtering out lower frequencies of the red noise, false periodicities arise in the global wavelet [33]. However, we do not really need to be sure with the detrended light curve confidence contour. Those were tools that led us to undeniable and self-consistent observation of a QPP in different wavelengths. Although the methods might be wrong, the result should not.

### 3.3.3 Flare energy estimation

One of the important results of a analysis of the solar flare should be the estimate of the energy released. We will now proceed to estimate the energy released by accelerated particles and plasma heating.

#### Thermal energy

For thermal energy we have

$$U = \frac{3}{2}k_B N_p T + \frac{3}{2}k_B N_e T \doteq 3k_B NT, \tag{3.3}$$

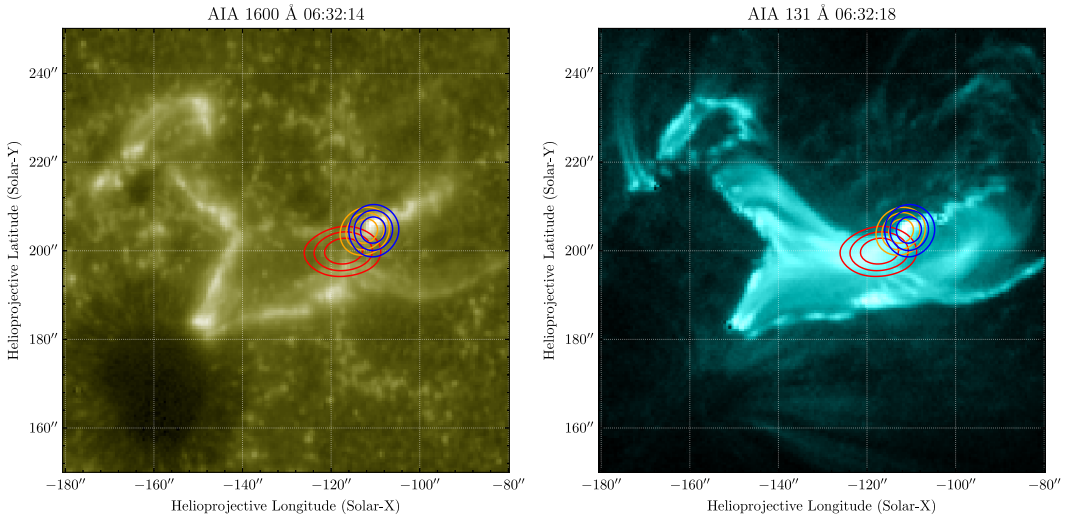


**Figure 3.10** Image reconstruciton of the third subinterval. This is the subinterval with lower flux at 32-63 keV, hence no source was reconstructed.

and number of particles can be computed from emission measure

$$Q = n^2 V = \frac{N^2}{V}, \tag{3.4}$$

so

$$U = 3k_B\sqrt{QV}T. \tag{3.5}$$

As we can see, to estimate the thermal energy, we need to estimate the volume of the thermal plasma first. But this is no simple deed, for we do not know which part of the plasma radiates. Thermal emission usually comes from a hot plasma at the top of the flare loop (the red region in Figure 1.8). We assume that this is our case and model its shape as a rotational ellipsoid. Now we only need to fit our 2d data with an ellipse. We do this using the principle component analysis. We fit the 2d intensity map with 2d normal distribution and use its axes as axes of our ellipse. But we still need to define the edge of the volume; we have the directions of the axes but not sizes. The sizes correspond to the variance of the Gaussian, so the question now is how do we choose the data for the fit. There are now three ways to proceed.

1. We only fit intensities above a constant multiplied by the square root of the integration time because of the Poisson noise. We choose the constant so that the ellipse corresponds to a 0.9 intensity contour in the first image. This would provide us with some absolute value so that we could easily compare our volumes. However, the data are already background subtracted and the noise is related to CLEAN algorithm, so the assumption of Poisson noise is not valid here.

2. We choose the threshold as a fraction of maximal intensity. However, we do this for every image separately, thus the comparison is dubious.

3. We combine those two methods. The mathematics behind this stays unclear, but it gives reasonable results.

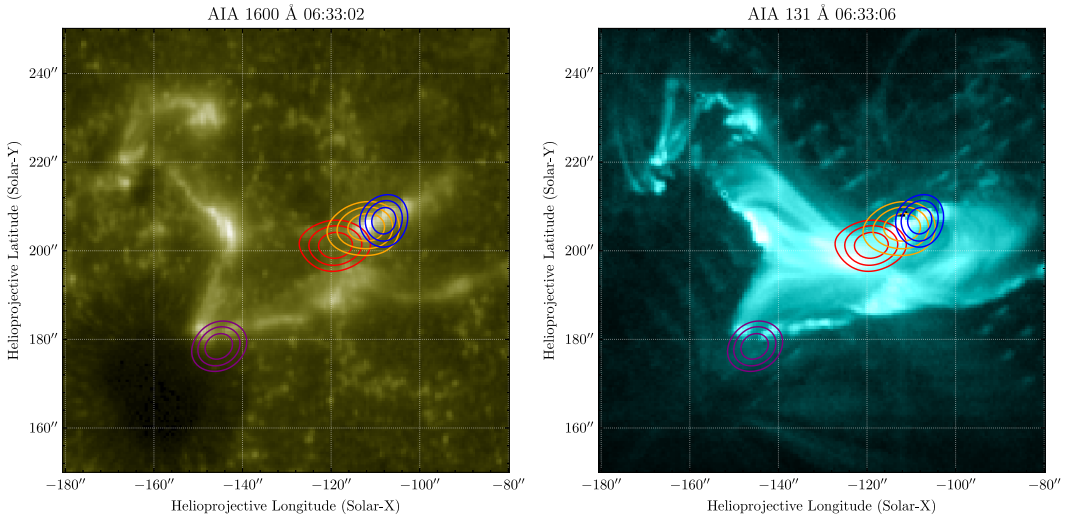


**Figure 3.11** Image reconstruction of the fourth subinterval. This corresponds to the second and highest peak (see Figure 3.3), so it was surprising to find no source at 32–63 keV near the western region. The image shows that the two distinct electron distributions described by the broken power-law correspond to spatially separate sources.

For a deeper discussion of this topic, see A.1. After estimating the volume, we can now calculate not only the thermal energy but also the density. That we can compare to plasma density from 1 GHz oscillation using the equation 1.72. As the plasma oscillation is only in the second subinterval we compare only one number. Plugging in $\omega_p = 1000$ MHz yeilds $n = 1.2 \times 10^{10}$ cm$^{-3}$. We get the value that we wanted to compare after substituting into the equation 3.4 the values from second subinterval. We get $n = 7.1 \times 10^{9}$ cm$^{-3}$, which is a bit more than half of the radio derived density. This calculation demonstrates that our estimation is not worthless.

### Nonthermal energy flux

Our work with thermal energy was made easier thanks to known results of thermodynamics; we knew the relation for energy. Now we have to calculate the energy from the electron distribution; from 1.47 we get

$$N = \int_{E_L}^{E_H} F\left(E_0\right) \mathrm{d}E_0 = \int_{E_L}^{E_H} K_1 E_0^{-\delta} \mathrm{d}E_0, \tag{3.6}$$

but for broken power-law we can write

$$\begin{aligned} F\left(E_0\right) = AE_0^{-\delta_L} \left(\Theta\left(E_0 - E_L\right) - \Theta\left(E_0 - E_B\right)\right) + \\ + BE_0^{-\delta_H} \left(\Theta\left(E_0 - E_B\right) - \Theta\left(E_0 - E_H\right)\right), \end{aligned} \tag{3.7}$$

where $\Theta\left(E_0\right)$ is the Heaviside function and $A, B$ are some constants such that

$$AE_B^{-\delta_L} = BE_B^{-\delta_H}, \tag{3.8}$$

therefore

$$N = \int_{E_L}^{E_H} F\left(E_0\right) \mathrm{d}E_0 = \int_{E_L}^{E_B} AE_0^{-\delta_L} \mathrm{d}E_0 + \int_{E_B}^{E_H} BE_0^{-\delta_H} \mathrm{d}E_0 \tag{3.9}$$

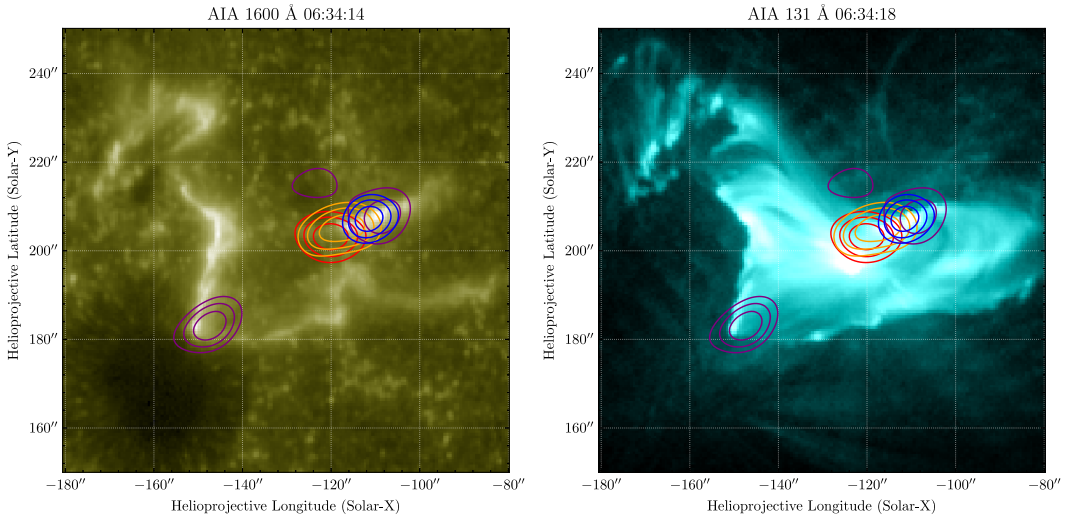


**Figure 3.12** Image reconstruction of the fifth time subinterval. Aside from usual sources there is a 70 % contour near the western region. This is probably an artifact due to low count statistic.

and from Equation 3.8 we get

$$A = \frac{N}{\int_{E_L}^{E_B} E_0^{-\delta_L} \mathrm{d}E_0 + E_0^{\delta_H - \delta_L} \int_{E_B}^{E_H} E_0^{-\delta_H} \mathrm{d}E_0}. \tag{3.10}$$

This is how we can find the exact electron distribution, Figure 3.22 is an example from the third time subinterval. After getting all the electron distributions, we just need to integrate them as in equation 3.6

$$f = \int_{E_L}^{E_H} E_0 F\left(E_0\right) \mathrm{d}E_0 \tag{3.11}$$

and then once more to get the actual nonthermal energy released.

$$E\left(T\right) = \int_{t_0}^{T} f \mathrm{d}t \tag{3.12}$$

Both flux and energy are in Figure 3.23

## 3.4 Results

Let us now step back and summarize our results to construct some consistent interpretation.

On light curves of HXR (Figure 3.3) and radio on 5 GHz (Figure 3.15) we discovered two distinct main peaks, first at 06:31:10 and second at 06:33:00. These are the first two peaks that Jebaraj et al. [27] report. The light curves at SXR and 13.1 nm evolve much more smoother and monotonously (see Figure 3.20), pointing to increase in emission from thermalised plasma. Both of these light curves are typical for the impulsive phase [12] the prior corresponding to the energy release itself and latter to the atmospheric response.

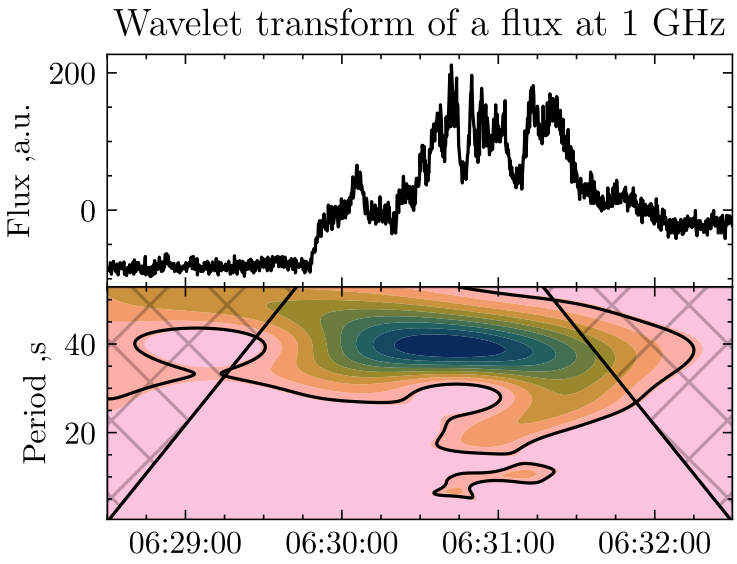


**Figure 3.13** Wavelet transform of Ondřejov data from 06:28:30-06:33:30 with 0.2s time step. Every step in contours is 10 % of the maximal value. We see three main peaks with period around 40 s. Second peak has two more lower quasi-periods thus becoming more fragmented

In chosen subintervals and after background subtraction we fitted the flux as a function of energy with a thermal, a nonthermal and an albedo component. Again, compared to Jebaraj et al. [27] our approach is focused more on the details as they did not use the albedo component, focusing on the broader picture (and ultimately different phenomena). From the residuals in Figures 3.6 and 3.7, we see that the thermal fit is problematic. This is not that surprising since we introduced strong assumptions such as fitting with single thermal component itself - there might be more than one thermalised particle population. Every subinterval besides the first one, we eventually fitted with broken power-law. This could generally mean many different things, such as the subintervals being too wide to catch the temporal changes in the flux or higher efficiency of accelerating electrons on lower energies. But our power-law is broken in the opposite direction than is typical; low delta is larger than high delta $\delta_H < \delta_L$. Normally, this might mean that something went wrong with the background subtraction. But that is probably not the case here as we tried different methods and kept getting the same result. It also lines up with the two peaks we saw and is backed up by the reconstructed images.

It is worth mentioning that it is clear from the EUV images that the flare has no simple topology, definitely not of the classical model of one loop with two footpoints from Figure 1.7.

We reconstructed images in the five subintervals corresponding to initial growth, first peak, middle pause, second peak, and decay. After reprojection on the EUV images we found that there is one HXR source in a close proximity to the sunspot in the southern part of the AR and second in the western part. There is also a SXR source near the western HXR source. As we used more energy subintervals, we were able to find that the southern source is much harder (i.e. has lower delta, thus is more efficient at accelerating electrons to higher energies), namely during the second flux peak. This is surprising because the stronger the magnetic field,

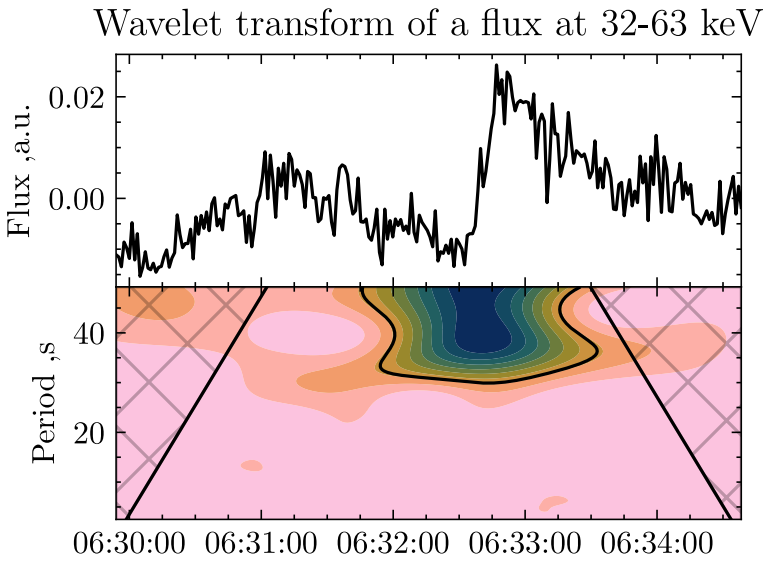


**Figure 3.14** Wavelet transform of HXR data from STIX.

the higher the mirror point; the HXR flux from the southern source should be lower. This result is similar to what Battaglia et al. published in [28]. They propose two possible interpretations:

1. The reconnection point was closer to the sunspot
2. The plasma has higher density near the weaker source, thus hindering the electrons in the corona so they lose energy before they can emit in the photosphere

The second reason would be supported by the fact that we found thermal X-ray emission in a proximity of the weaker HXR source. Nevertheless, this explains the unusual broken power-law; there are probably two different populations on different energies with different power-law index.

Majority of the fitted parameters in Figure 3.23 have no clear trend and are quite noisy. What we can see clearly is the rising emission measure which leads us to conclusion that due to low variation of the volumes, the density must be the cause of that rise of emission measure. However, it seems that our estimation was truly only for orientation, the physical reality is probably more complicated. One of the key problems of our analysis is the assumption of isothermal plasma. Not in the sense of uniform temperature but of one distribution. It is not unprobable that there are actually more thermalised populations. What we see in the AIA images is that the whole area was covered with hot plasma and two additional saturated blops can be seen near the western source. Also on our fits there is a clear trend in the residua in the thermal part of the spectrum (see Figures 3.6 and 3.7). This could be caused by a systematic error in the calibration of the instrument; there is a calibration line in the most problematic energy bin. However, we see that in the first fit where the background should be relatively strongest, the trend in residua is the weakest.

What is also a bit surprising is the constant temperature. This could be caused by the motion of the hot plasma; there is more and more plasma being heated to the same temperature rather than one reion of hot plasma being heated

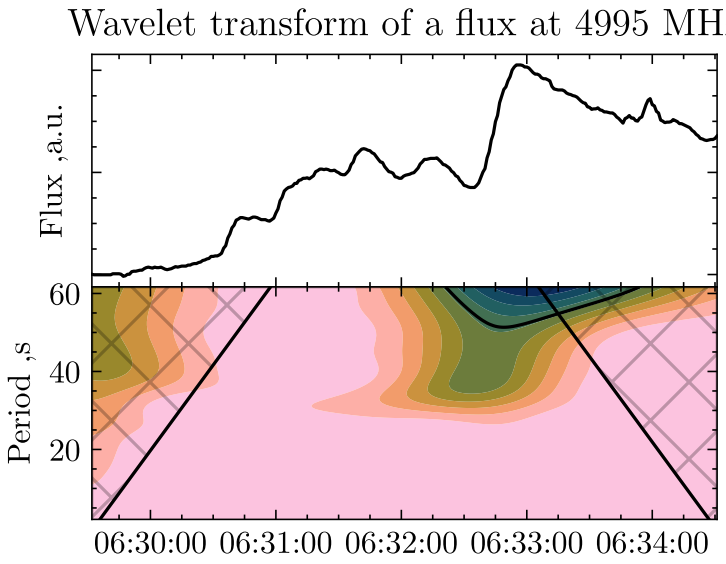


**Figure 3.15** Wavelet transform of radio data from Learmonth at 4995 MHz.

consistently. This would also point to the interpretation with more thermalised regions.

There is a faint increase in the electron flux during the two peaks in the Figure 3.23. They are definitely more articulated in the nonthermal energy flux, which shows in the nonthermal energy released as well. It seems like the thermal energy flux would be anticorrelated with the nonthermal one. This could be because of plasma heating after absorbing the fast electron energy. But the more probable explanation is that it is an artifact from how we determined the volumes; there was stronger nonthermal signal during the peaks, therefore higher residua and threshold and smaller volume. We see that the energy flux is around $10^{20}$ W which is the usual value as discussed at the end of the subsection 1.2.3. In that section we also derived that the energy partition $Q^{out}_{K/T}$ between kinetic and thermal energy should be 1. However, from Figure 3.23 we can see that $Q^{out}_{K/T} \approx 3$. Even though according to Jebaraj et al.[27] SEP event took place at the time so the kinetic energy should be even higher, the model itself is quite simplified ant the partition is often much more unbalanced [34]. Warmuth[34] summarizes the results of energy estimations of different flares from some set of observations. In their Figure 7 they show that the nonthermal energy of these observations was between $10^{23}$ and $10^{25}$ J for M1-2 flare. In Figure 1 we can see the peak thermal energy being in the interval of $10^{22}$ and $10^{24}$ J. These values are higher than ours but they should be (namely the peak thermal energy) as we analysed only first few minutes of the event. What is maybe more relevant are the volume estimates of these observations ranging from $10^{26}$ and $10^{28}$ cm$^{-3}$ for M1-2 flares which is exactly what we got with our simple method.

From wavelet analysis we found a quasi-period between 30-40 s. We found 3 pulses at 1 GHz at 06:30:05, 06:30:45, 06:31:17 UT whereas 5 peaks at 5 GHz at 06:30:41, 06:31:11, 06:31:40, 06:32:12 UT. The average period is 36 for 1 GHz and 35 s for 5 GHz. The HXR corresponds with 5 GHz. It is not surprising to find such a correspondence between HXR and microwave[35] but the plasma oscillation correspondence is not as usual. There are two main interpretations

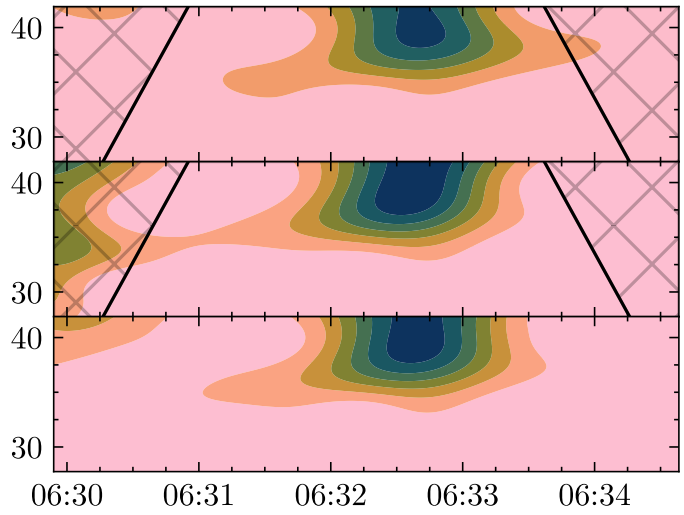


**Figure 3.16** *Top*: Wavelet power of HXR. *Mid*: wavelet power at 4995 MHz. Both of the wavelet powers are a bit different as they had to be trimmed to a common time interval and resampled to the highest time step. *Bottom*: crosswavelet of the two signals. The elongation near 35 seconds suggests a shared quasi-periodic feature in both light curves.

of QPP; it might be a MHD loop oscillation where the oscillations of HXR are caused by sausage instability changing the effect of the magnetic mirror in time, or a quasi-periodic electron injection[16]. Due to the fact that the magnetic mirror mechanism is not working as it should according to our analysis we prefer the second option. As we have shown the radio source at 1 GHz is probably at the loop top for two reasons: it has similar density as the SXR source based only on our rough estimation of the volume and plasma frequency and it has the same quasi-period as electrons traveling down the loop. This could mean that the periodically injected electrons disturb the thermal plasma causing the plasma oscillation. But there are temporal discrepancies: the times of 1 GHz peaks are around 5 s delayed (it should be the other way round) and the first 1 GHz peak is missing on the 5 GHz light curve. This could be explained by the first peak at 1 GHz being actually the first at 5 GHz (this is also supported by the fact that the first two periods have almost the same length 43-42 s and 32-30 s) which would, however, mean that it took around 35 s for the electrons to get down to photosphere which is far too much, or that the plasma oscillation is not caused by the injection but precedes it. But again, the electron beam that causes the thermal plasma to oscillate and thus loses its energy could at least partially explain the asymmetry of the HXR spectra.

### Future work

In our analysis we have found out *what* is going on and *when*. If we want to try to understand the event as a whole, it might be helpful to gather the information about where did those things happen.

We linked the plasma oscillation on 1 Ghz with the thermal SXR emission which we can localise but it is more of a speculation. Wavelet analysis of SXR imaging spectroscopy might serve as more evidence in case of high correlation

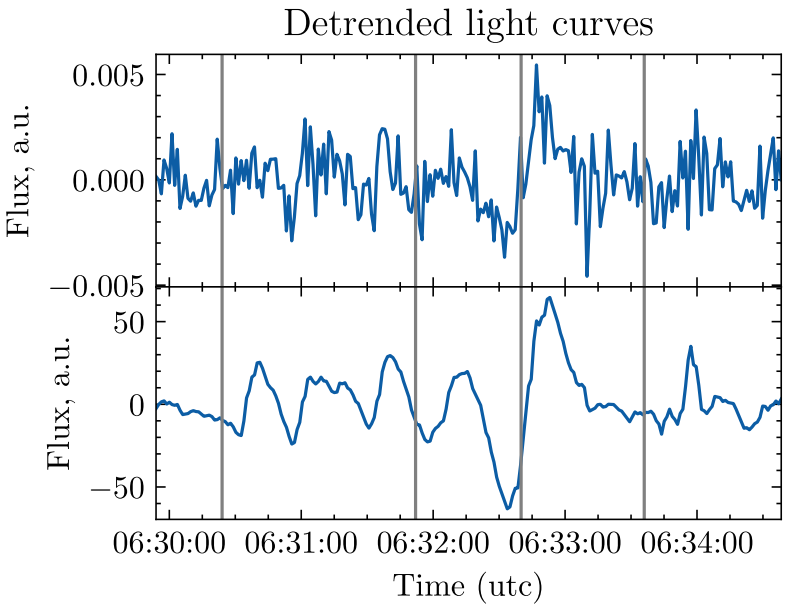


**Figure 3.17** Detrended light curves. The last 2 peaks at 1 GHz correspond to first two peaks here.

with the 1 GHz data. Unfortunately, we did not find any interferometers that gathered data of this event on this frequency, so the spatial information about the radio emission could not be retrieved.

There is another method that would inform us on the geometry of the event; using neural network for coronal magnetic field extrapolation. Jebaraj et al.[27] did this but include their results in the appendix and discusse them quite briefly. This could help us understand which magnetic field lines actually reconnected and whether there was some kind of asymetry in the field configuration itself (rather than in density etc.).

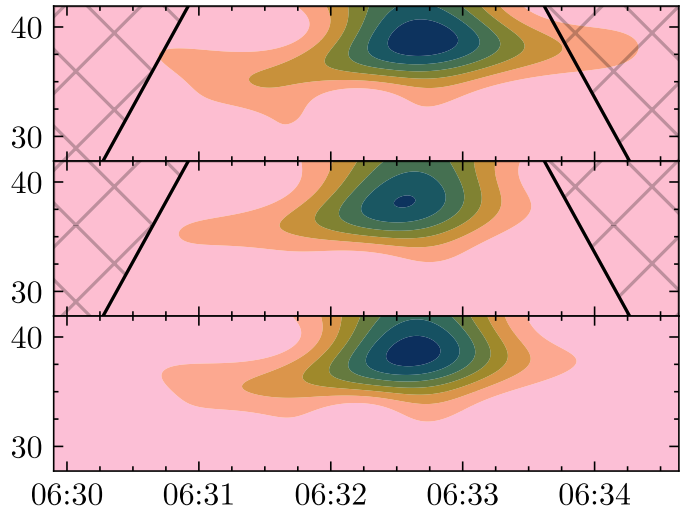


**Figure 3.18** Crosswavelet of detrended light curves

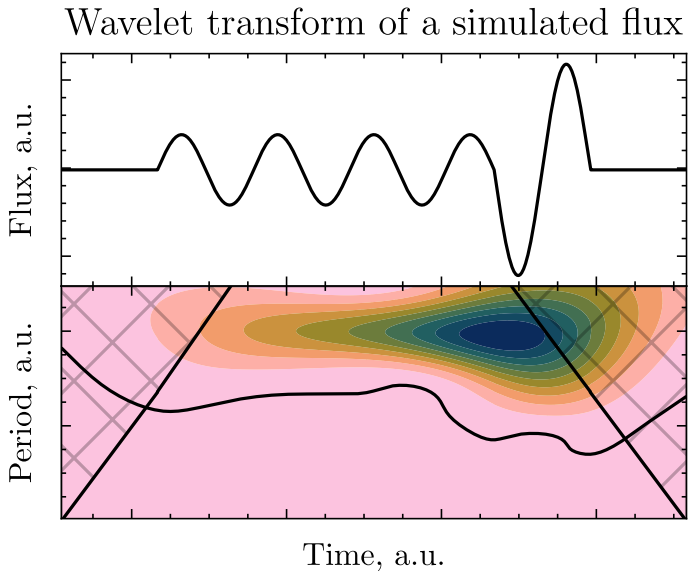


**Figure 3.19** Wavelet of a simulated signal with the last period having three times greater amplitude. We observe the shift of wavelet power in time although the period is the same throughout the interval.

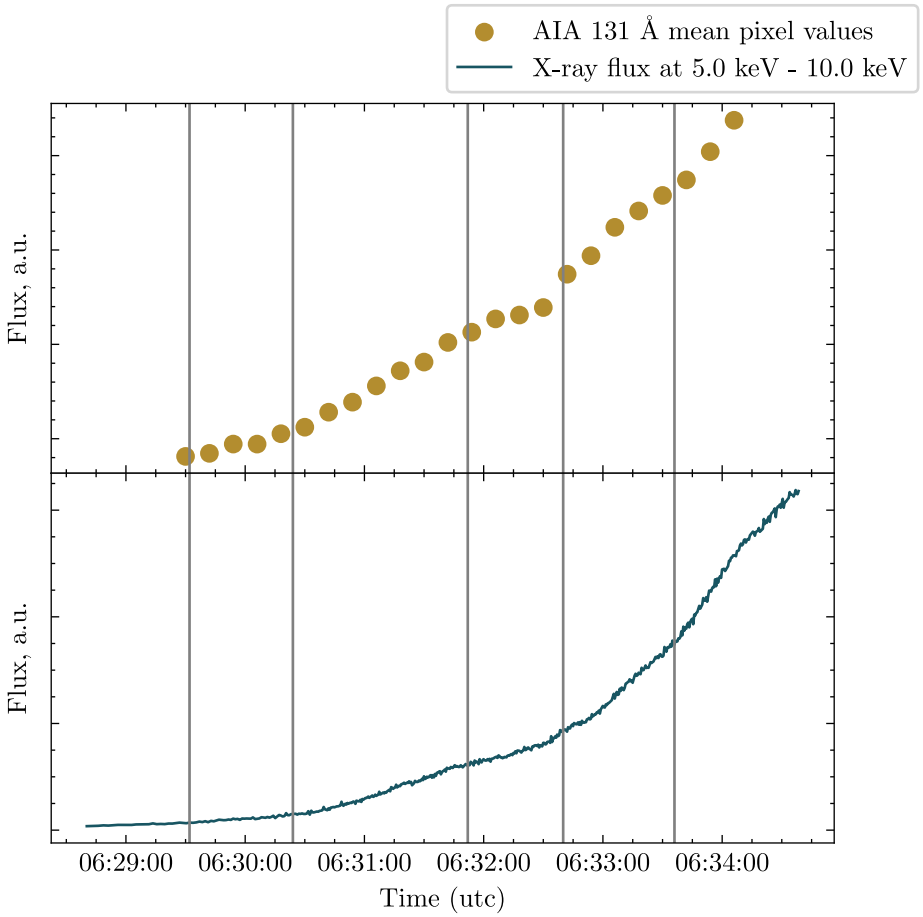


**Figure 3.20** The light curves from AIA 13.1 nm and SXR 5–10 keV are shown with marked imaging intervals. Even though the plot includes times before our main focus (which starts at 06:29:30 UT), the first subinterval only starts after that. The two curves look very similar overall, and even within each subinterval—like how both rise more slowly in the third subinterval between the two nonthermal peaks.

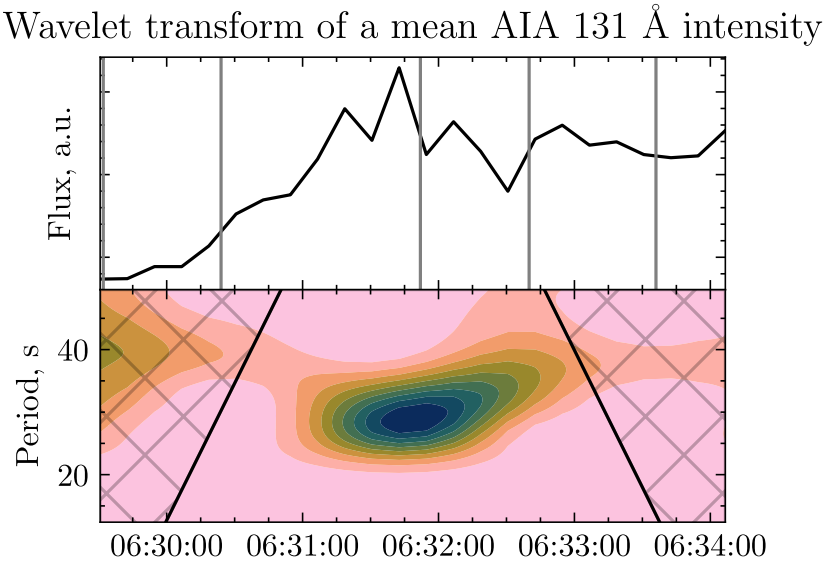


**Figure 3.21** Wavelet transform of the average pixel values from AIA 13.1 nm images, taken from a square region with corners at (-160”, 170”) and (-140”, 190”) in helioprojective coordinates (compare with Figure 3.11). The wavelet power is fairly weak and stays below the noise level, so no confidence contours appear. The time resolution is 12 seconds.

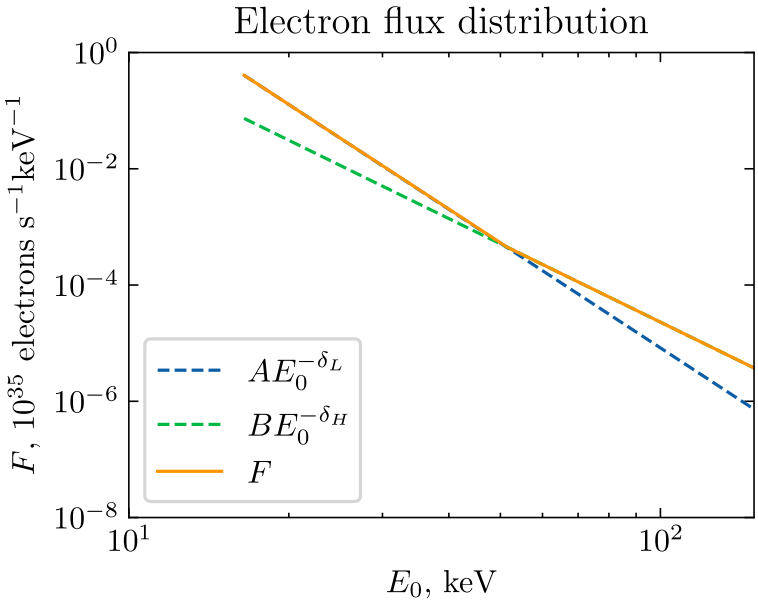


**Figure 3.22** Distributions of electrons losing their energy in the Sun atmosphere. By the full line we denote the spatially integrated measured distribution, the dashed lines show th two components of this spectrum. The softer one (steeper) we associate with the western source whereas the flatter (harder) with the southern source in Figure 3.11.

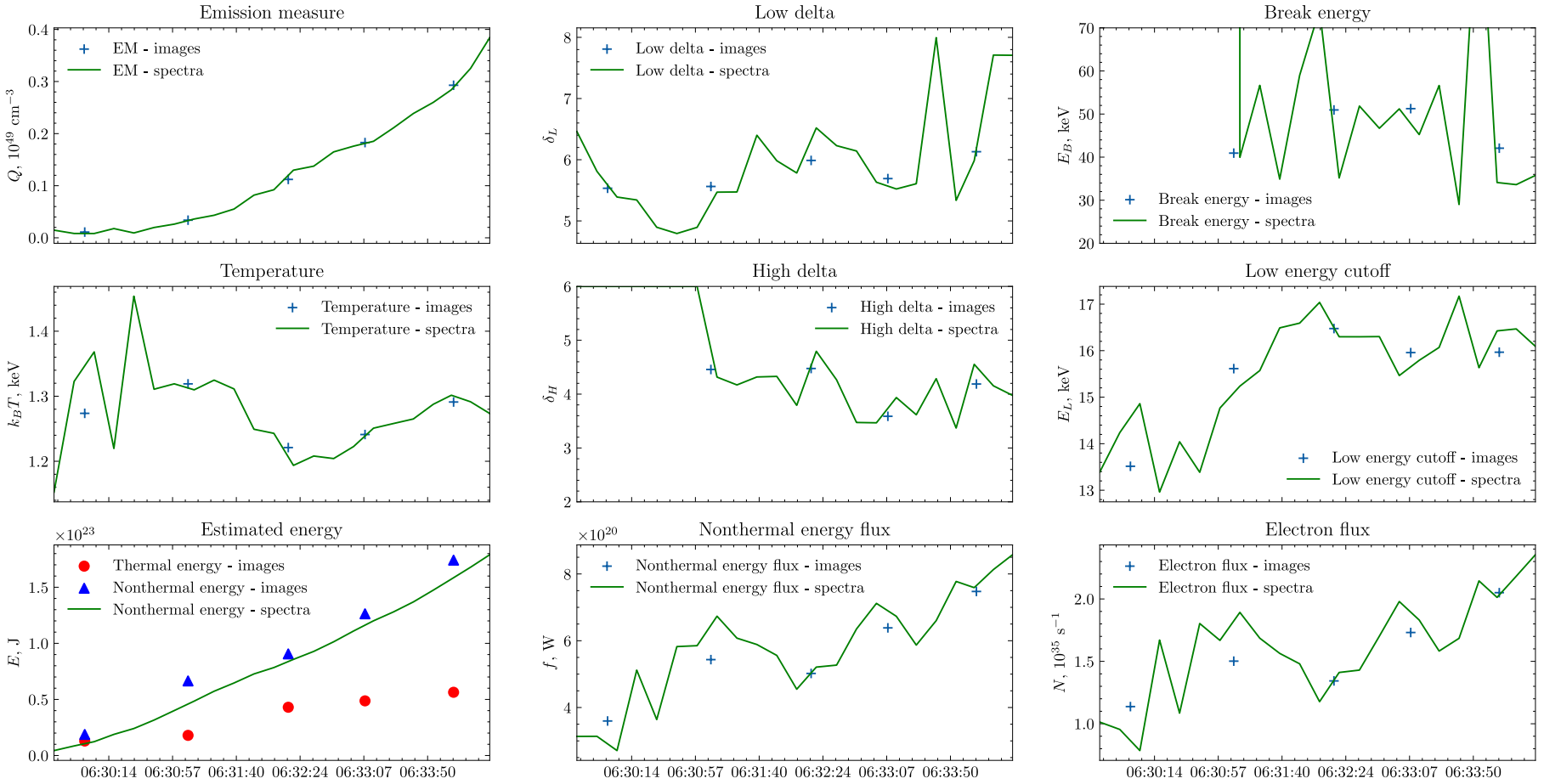


**Figure 3.23** Fitted parameters and calculated energies. The nonthermal energy is cumulative meaning that for each subinterval we sum the values of all preceeding subintervals. The thermal energy is not cumulative, all the values are the thermal energy only in that subinterval. This is not nonsensical as the thermal energy itself is cumulative in this time scale; the thermal energy in each subinterval is also result of heating in the intervals before.

# Conclusion

Let us now review our results in the context of the aims of the work.

We have compiled a brief introduction to the physics of solar flares based on available literature, covering the fundamental MHD equations, the Sweet-Parker model of solar flares, and various mechanisms responsible for electromagnetic emission.

We adapted existing software tools for the analysis of X-ray data from STIX, EUV data from AIA, and radio observations from Ondřejov and Learmonth to suit the specific requirements of our study. This was done in python and IDL

We applied this software on the event from 2021-10-09 in order to better understand the course of the impulsive phase. We analysed X-ray spectra, reconstructed X-ray sources, reprojected them on EUV images. At the same time we investigated multiple light curves using wavelet analysis.

We found that the spatial distribution of the X-ray emission was notably asymmetric in terms of spectral hardness. During the peak X-ray flux, the two main HXR regions appeared in different spectral bands, consistent with the spatially integrated spectrum exhibiting a broken power-law, suggesting two distinct electron populations. In addition, we identified a quasi-periodic signal across fluxes in different wavelengths, which may serve as a basis for further investigation.

*Acknowledgements* Solar Orbiter is a space mission of international collaboration between ESA and NASA, operated by ESA. The STIX instrument is an international collaboration between Switzerland, Poland, France, Czech Republic, Germany, Austria, Ireland, and Italy. [36][37]

SDO data are provided courtesy of NASA/SDO and the AIA, EVE, and HMI science teams.

This research used version 6.1.1 [38] of the SunPy open source software package [30].

Wavelet software was provided by C. Torrence and G. Compo, and is available at URL: `http://atoc.colorado.edu/research/wavelets/`.

We found Figures 1.7 and 1.8 thanks to Grand Archive of Flare and CME Cartoons `https://www.astro.gla.ac.uk/cartoons/index.html`

We used SciencePlots [39] and cmcrameri [40] [39] for plotting in python.

ChatGPT was used throughout all stages of this work: for the literature search, theoretical discussion, debugging of Python and IDL scripts, formatting LaTeX, and rephrasing of unclear formulations.

# Bibliography


1. Vanýsek, Vladimír. *Základy astronomie a astrofyziky*. Praha: Academia, 1980.
2. Budějický, Jaromír; Plavec, Miroslav; Plavcová, Zdeňka. *Radioastronomie*. Praha: Státní pedagogické nakladatelství, 1962.
3. Foukal, Peter. *Solar Astrophysics*. 2nd. Wiley-VCH, 2004. ISBN 9783527404283.
4. Shapiro, Alexander I.; Peter, Hardi; Solanki, Sami K. The Sun's Atmosphere. In: Engvold, Oddbjørn; Vial, Jean-Claude; Skumanich, Andrew (eds.). *The Sun as a Guide to Stellar Physics*. Elsevier, 2019, pp. 59–96. Available from DOI: 10.1016/B978-0-12-814334-6.00003-0.
5. Stix, Michael. *The Sun: An Introduction*. 2nd. Springer, 2004. ISBN 9783540207411.
6. Lang, Kenneth R. *The sun from space*. Berlin, Germany: Springer, 2000. Astronomy and Astrophysics Library.
7. Karlický, M. *Plasma astrophysics*. Prague: MatfyzPress, 2014.
8. Kulhánek, P. *Vybrané kapitoly z teoretické fyziky III*. Prague: AGA, 2020.
9. Priest, E.R. *Magnetohydrodynamics: Overview*. Oxford University Press, 2020. ISBN 9780190871994. Available from DOI: 10.1093/acrefore/9780190871994.013.6.
10. Martens, P. C. H.; Kuin, N. P. M. A circuit model for filament eruptions and two-ribbon flares. *Solar Physics*. 1989, vol. 122, no. 2, pp. 263–302. ISSN 1573-093X. Available from DOI: 10.1007/bf00912996.
11. Kontar, E. P.; Perez, J. E.; Harra, L. K.; Kuznetsov, A. A.; Emslie, A. G.; Jeffrey, N. L. S.; Bian, N. H.; Dennis, B. R. Turbulent Kinetic Energy in the Energy Balance of a Solar Flare. *Physical Review Letters*. 2017, vol. 118, no. 15. ISSN 1079-7114. Available from DOI: 10.1103/physrevlett.118.155101.
12. Tandberg-Hanssen, Einar; Emslie, A. Gordon. *The Physics of Solar Flares*. Vol. 12. Cambridge University Press, 1988. Cambridge Astrophysics Series. ISBN 9780521115520.
13. Magdziarz, Paweł; Zdziarski, Andrzej A. Angle-dependent Compton reflection of X-rays and gamma-rays. *Monthly Notices of the Royal Astronomical Society*. 1995, vol. 273, no. 3, pp. 837–848. ISSN 1365-2966. Available from DOI: 10.1093/mnras/273.3.837.
14. Kontar, E. P.; MacKinnon, A. L.; Schwartz, R. A.; Brown, J. C. Compton backscattered and primary X-rays from solar flares: angle dependent Green's function correction for photospheric albedo. *Astronomy amp; Astrophysics*. 2006, vol. 446, no. 3, pp. 1157–1163. ISSN 1432-0746. Available from DOI: 10.1051/0004-6361:20053672.
15. Ginzburg, V. L.; Syrovatskii, S. I. Cosmic Magnetobremsstrahlung (Synchrotron Radiation). *Annual Review of Astronomy and Astrophysics*. 1965, vol. 3, no. 1, pp. 297–350. ISSN 1545-4282. Available from DOI: 10.1146/annurev.aa.03.090165.001501.

16. Nakariakov, V. M.; Pilipenko, V.; Heilig, B.; Jelínek, P.; Karlický, M.; Klimushkin, D. Y.; Kolotkov, D. Y.; Lee, D.-H.; Nisticò, G.; Van Doorsselaere, T.; Verth, G.; Zimovets, I. V. Magnetohydrodynamic Oscillations in the Solar Corona and Earth's Magnetosphere: Towards Consolidated Understanding. *Space Science Reviews*. 2016, vol. 200, no. 1–4, pp. 75–203. ISSN 1572-9672. Available from DOI: 10.1007/s11214-015-0233-0.

17. Torrence, Christopher; Compo, Gilbert P. A Practical Guide to Wavelet Analysis. *Bulletin of the American Meteorological Society*. 1998, vol. 79, no. 1, pp. 61–78. Available from DOI: 10.1175/1520-0477(1998)079<0061:APGTWA>2.0.CO;2.

18. Müller, D.; St. Cyr, O. C.; Zouganelis, I.; Gilbert, H. R.; Marsden, R.; Nieves-Chinchilla, T.; Antonucci, E.; Auchère, F.; Berghmans, D.; Horbury, T. S.; Howard, R. A.; Krucker, S.; Maksimovic, M.; Owen, C. J.; Rochus, P.; Rodriguez-Pacheco, J.; Romoli, M.; Solanki, S. K.; Bruno, R.; Carlsson, M.; Fludra, A.; Harra, L.; Hassler, D. M.; Livi, S.; Louarn, P.; Peter, H.; Schühle, U.; Teriaca, L.; del Toro Iniesta, J. C.; Wimmer-Schweingruber, R. F.; Marsch, E.; Velli, M.; De Groof, A.; Walsh, A.; Williams, D. The Solar Orbiter mission. Science overview. *Astronomy and Astrophysics*. 2020, vol. 642, A1. Available from DOI: 10.1051/0004-6361/202038467.

19. Massa, Paolo; Hurford, G. J.; Volpara, Anna; Kuhar, Matej; Battaglia, Andrea Francesco; Xiao, Hualin; Casadei, Diego; Perracchione, Emma; Garbarino, Sara; Guastavino, Sabrina; Collier, Hannah; Dickson, Ewan C. M.; Emslie, A. Gordon; Ryan, Daniel F.; Maloney, Shane A.; Schuller, Frederic; Warmuth, Alexander; Massone, Anna Maria; Benvenuto, Federico; Piana, Michele; Krucker, Säm. The STIX Imaging Concept. *Solar Physics*. 2023, vol. 298. Available also from: https://api.semanticscholar.org/CorpusID:263625230.

20. Hayes, Laura A.; Musset, Sophie; Müller, Daniel; Krucker, Säm. The Spectrometer Telescope for Imaging X-Rays (STIX) on Solar Orbiter. In: Bambi, Cosimo; Sangangelo, Andrea (eds.). *Handbook of X-ray and Gamma-ray Astrophysics*. 2022, p. 96. Available from DOI: 10.1007/978-981-16-4544-0_168-1.

21. Högbom, J. A. Aperture Synthesis with a Non-Regular Distribution of Interferometer Baselines. *Astronomy and Astrophysics, Supplement*. 1974, vol. 15, p. 417.

22. Pesnell, W. Dean; Thompson, B. J.; Chamberlin, P. C. The Solar Dynamics Observatory (SDO). *Solar Physics*. 2012, vol. 275, no. 1-2, pp. 3–15. Available from DOI: 10.1007/s11207-011-9841-3.

23. Lemen, James R.; Title, Alan M.; Akin, David J.; Boerner, Paul F.; Chou, Catherine; Drake, Jerry F.; Duncan, Dexter W.; Edwards, Christopher G.; Friedlaender, Frank M.; Heyman, Gary F.; Hurlburt, Neal E.; Katz, Noah L.; Kushner, Gary D.; Levay, Michael; Lindgren, Russell W.; Mathur, Dnyanesh P.; McFeaters, Edward L.; Mitchell, Sarah; Rehse, Roger A.; Schrijver, Carolus J.; Springer, Larry A.; Stern, Robert A.; Tarbell, Theodore D.; Wuelser, Jean-Pierre; Wolf-

son, C. Jacob; Yanari, Carl; Bookbinder, Jay A.; Cheimets, Peter N.; Caldwell, David; Deluca, Edward E.; Gates, Richard; Golub, Leon; Park, Sang; Podgorski, William A.; Bush, Rock I.; Scherrer, Philip H.; Gummin, Mark A.; Smith, Peter; Auker, Gary; Jerram, Paul; Pool, Peter; Soufli, Regina; Windt, David L.; Beardsley, Sarah; Clapp, Matthew; Lang, James; Waltham, Nicholas. The Atmospheric Imaging Assembly (AIA) on the Solar Dynamics Observatory (SDO). *Solar Physics*. 2012, vol. 275, no. 1-2, pp. 17–40. Available from doi: 10.1007/s11207-011-9776-8.

24. Boerner, Paul; Edwards, Christopher; Lemen, James; Rausch, Adam; Schrijver, Carolus; Shine, Richard; Shing, Lawrence; Stern, Robert; Tarbell, Theodore; Title, Alan; Wolfson, C. Jacob; Soufli, Regina; Spiller, Eberhard; Gullikson, Eric; McKenzie, David; Windt, David; Golub, Leon; Podgorski, William; Testa, Paola; Weber, Mark. Initial Calibration of the Atmospheric Imaging Assembly (AIA) on the Solar Dynamics Observatory (SDO). *Solar Physics*. 2012, vol. 275, no. 1-2, pp. 41–66. Available from doi: 10.1007/s11207-011-9804-8.

25. NASA Solar Dynamics Observatory. *HMI and AIA Spectral Bands*. n.d. Available also from: https://sdo.gsfc.nasa.gov/data/channels.php. Accessed: 2025-02-28.

26. Battaglia, Andrea Francesco; Hudson, Hugh; Warmuth, Alexander; Collier, Hannah; Jeffrey, Natasha L. S.; Caspi, Amir; Dickson, Ewan C. M.; Saqri, Jonas; Purkhart, Stefan; Veronig, Astrid M.; Harra, Louise; Krucker, Säm. The existence of hot X-ray onsets in solar flares. *Astronomy amp; Astrophysics*. 2023, vol. 679, A139. issn 1432-0746. Available from doi: 10.1051/0004-6361/202347706.

27. Jebaraj, Immanuel C.; Kouloumvakos, A.; Dresing, N.; Warmuth, A.; Wijsen, N.; Palmroos, C.; Gieseler, J.; Marmyleva, A.; Vainio, R.; Krupar, V.; Wiegelmann, T.; Magdalenic, J.; Schuller, F.; Battaglia, A. F.; Fedeli, A. Multiple injections of energetic electrons associated with the flare and CME event on 9 October 2021. *Astronomy amp; Astrophysics*. 2023, vol. 675, A27. issn 1432-0746. Available from doi: 10.1051/0004-6361/202245716.

28. Battaglia, Andrea Francesco; Krucker, Säm; Veronig, Astrid M.; Stiefel, Muriel Zoë; Warmuth, Alexander; Benz, Arnold O.; Ryan, Daniel F.; Collier, Hannah; Harra, Louise. The observational evidence that all microflares that accelerate electrons to high energies are rooted in sunspots. *Astronomy amp; Astrophysics*. 2024, vol. 691, A172. issn 1432-0746. Available from doi: 10.1051/0004-6361/202451152.

29. Barnes, Will T.; Cheung, Mark C. M.; Bobra, Monica G.; Boerner, Paul F.; Chintzoglou, Georgios; Leonard, Drew; Mumford, Stuart J.; Padmanabhan, Nicholas; Shih, Albert Y.; Shirman, Nina; Stansby, David; Wright, Paul J. aiapy: A Python Package for Analyzing Solar EUV Image Data from AIA. *Journal of Open Source Software*. 2020, vol. 5, no. 55, p. 2801. Available from doi: 10.21105/joss.02801.

30. The SunPy Community; Barnes, Will T.; Bobra, Monica G.; Christe, Steven D.; Freij, Nabil; Hayes, Laura A.; Ireland, Jack; Mumford, Stuart; Perez-Suarez, David; Ryan, Daniel F.; Shih, Albert Y.; Chanda, Prateek; Glogowski, Kolja; Hewett, Russell; Hughitt, V. Keith; Hill, Andrew; Hiware, Kaustubh; Inglis, Andrew; Kirk, Michael S. F.; Konge, Sudarshan; Mason, James Paul; Maloney, Shane Anthony; Murray, Sophie A.; Panda, Asish; Park, Jongyeob; Pereira, Tiago M. D.; Reardon, Kevin; Savage, Sabrina; Sipőcz, Brigitta M.; Stansby, David; Jain, Yash; Taylor, Garrison; Yadav, Tannmay; Rajul; Dang, Trung Kien. The SunPy Project: Open Source Development and Status of the Version 1.0 Core Package. *The Astrophysical Journal*. 2020, vol. 890, pp. 68–. Available from doi: 10.3847/1538-4357/ab4f7a.

31. Karlický, Marian; Rybák, Ján; Monstein, Christian. Fourier Power Spectra of Solar Noise Storms. *Solar Physics*. 2018, vol. 293, no. 10. issn 1573-093X. Available from doi: 10.1007/s11207-018-1367-5.

32. Inglis, A. R.; Ireland, J.; Dominique, M. QUASI-PERIODIC PULSATIONS IN SOLAR AND STELLAR FLARES: RE-EVALUATING THEIR NATURE IN THE CONTEXT OF POWER-LAW FLARE FOURIER SPECTRA. *The Astrophysical Journal*. 2015, vol. 798, no. 2, p. 108. issn 1538-4357. Available from doi: 10.1088/0004-637x/798/2/108.

33. Auchère, F.; Froment, C.; Bocchialini, K.; Buchlin, E.; Solomon, J. ON THE FOURIER AND WAVELET ANALYSIS OF CORONAL TIME SERIES. *The Astrophysical Journal*. 2016, vol. 825, no. 2, p. 110. issn 1538-4357. Available from doi: 10.3847/0004-637x/825/2/110.

34. Warmuth, A.; Mann, G. Thermal-nonthermal energy partition in solar flares derived from X-ray, EUV, and bolometric observations: Discussion of recent studies. *Astronomy amp; Astrophysics*. 2020, vol. 644, A172. issn 1432-0746. Available from doi: 10.1051/0004-6361/202039529.

35. White, S. M.; Benz, A. O.; Christe, S.; Fárník, F.; Kundu, M. R.; Mann, G.; Ning, Z.; Raulin, J.-P.; Silva-Válio, A. V. R.; Saint-Hilaire, P.; Vilmer, N.; Warmuth, A. The Relationship Between Solar Radio and Hard X-ray Emission. *Space Science Reviews*. 2011, vol. 159, no. 1–4, pp. 225–261. issn 1572-9672. Available from doi: 10.1007/s11214-010-9708-1.

36. Krucker, Säm; Hurford, G. J.; Grimm, O.; Kögl, S.; Gröbelbauer, H.-P; Etesi, L.; Casadei, D.; Csillaghy, A.; Benz, A. O.; Arnold, N. G.; Molendini, F.; Orleanski, P.; Schori, D.; Xiao, H.; Kuhar, M.; Hochmuth, N.; Felix, S.; Schramka, F.; Marcin, S.; Kobler, S.; Iseli, L.; Dreier, M.; Wiehl, H. J.; Kleint, L.; Battaglia, M.; Lastufka, E.; Sathiapal, H.; Lapadula, K.; Bednarzik, M.; Birrer, G.; Stutz, St.; Wild, Ch.; Marone, F.; Skup, K. R.; Cichocki, A.; Ber, K.; Rutkowski, K.; Bujwan, W.; Juchnikowski, G.; Winkler, M.; Darmetko, M.; Michalska, M.; Seweryn, K.; Białek, A.; Osica, P.; Sylwester, J.; Kowalinski, M.; Ścisłowski, D.; Siarkowski, M.; Stęślicki, M.; Mrozek, T.; Podgórski, P.; Meuris, A.; Limousin, O.; Gevin, O.; Le Mer, I.; Brun, S.; Strugarek, A.; Vilmer, N.; Musset, S.; Maksimović, M.; Fárník, F.; Kozáček, Z.; Kašparová, J.; Mann,

G.; Önel, H.; Warmuth, A.; Rendtel, J.; Anderson, J.; Bauer, S.; Dionies, F.; Paschke, J.; Plüschke, D.; Woche, M.; Schuller, F.; Veronig, A. M.; Dickson, E. C. M.; Gallagher, P. T.; Maloney, S. A.; Bloomfield, D. S.; Piana, M.; Massone, A. M.; Benvenuto, F.; Massa, P.; Schwartz, R. A.; Dennis, B. R.; Beek, H. F. van; Rodríguez-Pacheco, J.; Lin, R. P. The Spectrometer/Telescope for Imaging X-rays (STIX). *Astronomy amp; Astrophysics*. 2020, vol. 642, A15. ISSN 1432-0746. Available from DOI: 10.1051/0004-6361/201937362.

37. Xiao, Hualin; Maloney, Shane; Krucker, Säm; Dickson, Ewan; Massa, Paolo; Lastufka, Erica; Francesco Battaglia, Andrea; Etesi, László; Hochmuth, Nicky; Schuller, Frédéric; Ryan, Daniel F.; Limousin, Olivier; Collier, Hannah; Warmuth, Alexander; Piana, Michele. The data center for the Spectrometer and Telescope for Imaging X-rays (STIX) on board Solar Orbiter. *Astronomy amp; Astrophysics*. 2023, vol. 673, A142. ISSN 1432-0746. Available from DOI: 10.1051/0004-6361/202346031.

38. Mumford, Stuart J.; Freij, Nabil; Stansby, David. *sunpy: A Core Package for Solar Physics*. Zenodo, 2025. Available from DOI: 10.5281/ZENODO.14919949.

39. Garrett, John D. garrettj403/SciencePlots. 2021. Available from DOI: 10.5281/zenodo.4106649.

40. Crameri, Fabio. *Scientific colour maps*. Zenodo, 2023. Available from DOI: 10.5281/ZENODO.1243862.

41. Massa, Paolo; Schwartz, Richard; Tolbert, A. Kim; Massone, Anna Maria; Dennis, Brian R.; Piana, Michele; Benvenuto, Federico. MEM_GE: A New Maximum Entropy Method for Image Reconstruction from Solar X-Ray Visibilities. *The Astrophysical Journal*. 2020, vol. 894, no. 1, p. 46. Available from DOI: 10.3847/1538-4357/ab8637.

# List of Figures

# List of Tables

# List of Abbreviations

| | |
|---|---|
| AIA | Atmospheric Imaging Assembly. 30, 32, 35, 41, 47, 52, 53, 55, 63 |
| AR | Active Region. 32, 42, 46 |
| BKG | background. 26, 27, 34, 61 |
| CFL | Coarse flare location. 26, 27, 61 |
| CME | Coronal Mass Ejection. 33 |
| DEM | Detector/Electronics Module. 25, 61 |
| EUV | Extreme ultraviolet. 6, 13, 30, 31, 35, 46, 55, 61 |
| HXR | Hard X-ray. 16, 32, 33, 35–37, 39, 41, 42, 45–49, 55, 62, 63, 69 |
| IDL | Interactive Data Language. 33, 35, 55 |
| MHD | Magnetohydrodynamic. 7, 49, 55 |
| OSPEX | Object Spectral Executive. 33, 34 |
| QPP | Quasi Periodic Pulses. 22, 38, 39, 41, 42, 49 |
| RSTN | Radio Solar Telescope Network. 31, 39 |
| SDO | Solar Dynamics Observatory. 29, 35 |
| SEP | Solar Energetic Particles. 33, 48 |
| SOLO | Solar Orbiter. 25, 32, 35, 62 |
| STIX | Spectrometer/Telescope for Imaging X-rays. 25, 26, 29, 32, 33, 35, 37, 47, 55, 62 |
| SXR | Soft X-ray. 13, 16, 36, 37, 42, 45, 46, 49, 52, 63, 66 |
| vth | Variable Thermal. 34, 35, 38, 62 |

# A Appendix

## A.1 Choosing threshold for PCA data input

First we inspect how the data look in 3 dimensions. In Figure A.1 the SXR

**Figure A.1** The SXR data plotted in 3 dimensions. On top is the first subinterval, in the bottom is the fourth one.

data are plotted in 3 dimensions. The figure on the left is from data roughly from the first time subinterval, the figure on the right is from the fourth. From this figure it it very likely that the volume does not change, only the intensity of the signal. We considered three methods for choosing the threshold for PCA input data:

1. Constant multiplied by the square root of the integration time because of the Poisson noise. We choose the constant so that the ellipse corresponds to a 0.9 intensity contour in the first image. This gives us volumes plotted on Figure A.2 This estimate fails because, although the shape of the emission

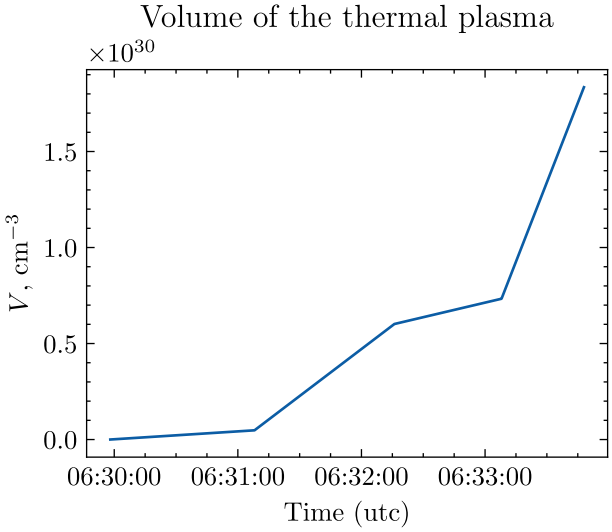


**Figure A.2** Volume of thermal plasma in time using the first method. The volumes are too high and the trend does not correspond to what we see in Figure A.1.

in Figure A.1 remains unchanged, its intensity increases significantly — to

the extent that the peak intensity in the first subinterval is comparable to the noise level in the fourth.

2. Fraction of maximal intensity. This gives us the volumes shown in Figure A.3 However, if we compare with the lengths of time subinterval, there is a clear correlation. This leads to the final method.

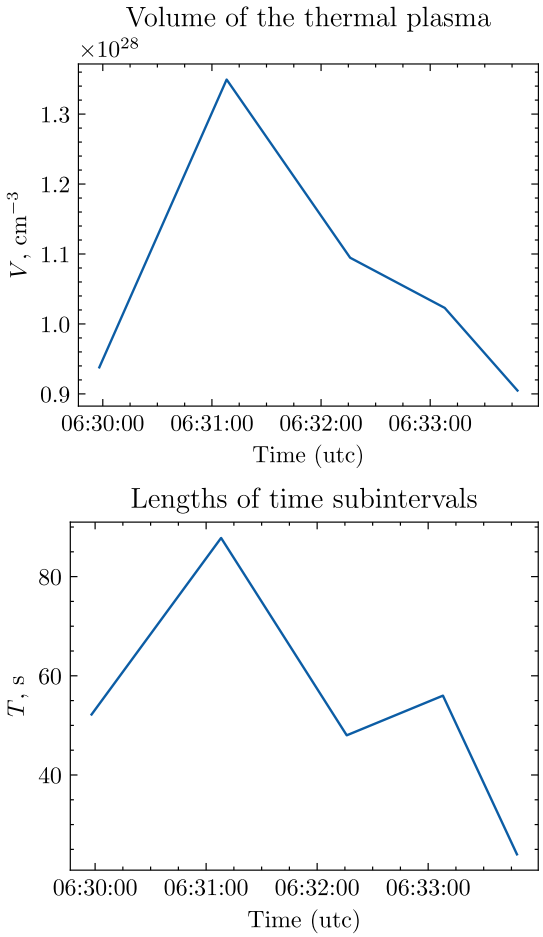


**Figure A.3** Volume of thermal plasma in time using the second method (top). Lengths of imaging subintervals (bottom). There is a clear and logical correlation.

3. Fraction of maximal intensity multiplied by the square root of the integration time. This method gives us volumes of reasonable magnitude and time evolution as demonstrated in Figure A.4 that we use in our analysis.

### MEM GE[41]

MEM stands for maximum entropy method. Same as in the direct back projection case in Subsection 2.1.1 we look for inverse of

$$\mathbf{v} = \mathbf{F}\mathbf{x} \tag{A.1}$$

where $\mathbf{v}$ is the vector of visibilities, $\mathbf{v} \in \mathbb{C}^{30}$, the photon flux $\mathbf{x}$ which is $N \times N$ is transformed to be a vector $\mathbf{x} \in \mathbb{R}^{N^2}$ and $\mathbf{F}$ is the matrix for DFT. The idea is to

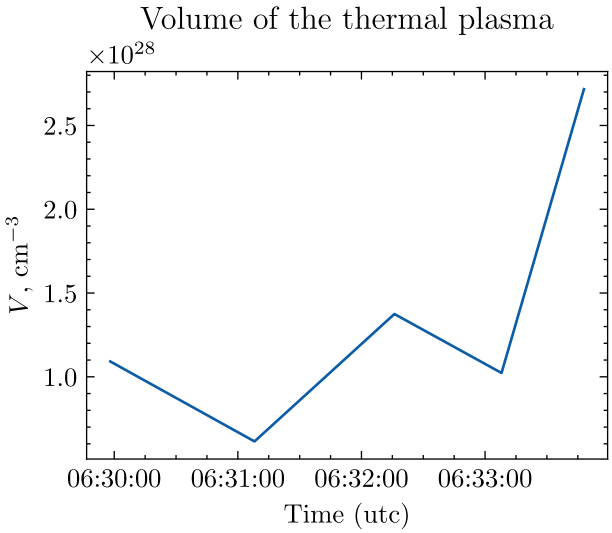


**Figure A.4** Volume of thermal plasma in time using the third method. This is what we use in our analysis

combine entropy maximization, least squares method, and physical constraints. We have

$$H = -\sum_{j=1}^{N^2} x_j \log\left(\frac{N^2 x_j}{Fe}\right) \tag{A.2}$$

where $e$ is the Euler number and $F$ is the total flux. Furthermore

$$\chi^2 = \sum_{i=1}^{30} \frac{(\mathbf{Fx})_i - v_i}{\sigma^2} - 30 \tag{A.3}$$

where $\sigma$ is the vector of experimental uncertainties, and finally

$$\Sigma_F = \sum_{j=1}^{N^2} x_j - F \tag{A.4}$$

For these quantities we have 3 constraints (one for best solution, two for physical solution)

$$\chi^2 = 0 \tag{A.5}$$

$$\Sigma_F = 0 \tag{A.6}$$

$$x_j \geq 0, \forall x_j \tag{A.7}$$

and we find

$$\arg\min_{\mathbf{x}} \left\{\chi^2 - \lambda H\right\} \tag{A.8}$$

where $\lambda$ is a Lagrange multiplier. This is implemented by iterating minimizing $\chi^2$ and then maximizing $H$ to fulfill all the constraints.

This method gives smooth solutions which are systematically super-resolved.

## A.2 Detrending light curves

For each light curve we can write

$$I_{QPP}(t) = I_{tot} - I_{trend}, \tag{A.9}$$

where $I_{QPP}$ is the quasi-periodic signal, $I_{tot}$ is the total flux and $I_{trend}$ is the global trend of the light curve. The question is: how do we determine the global trend of the light curve?

This might not be a major issue, since we already used the global trends in light curves to define time subintervals (see Figure 3.3). However, quantifying this trend is less straightforward. Our approach was loosely inspired by concepts such as the Central Limit Theorem and the heat equation, though interpreted in a simplified, intuitive way. The key observation is this: convolution of the signal with a Gaussian kernel produces a smoothed version of the signal. The degree of smoothing depends on the variance of the Gaussian. As the variance approaches zero, the Gaussian becomes more like a Dirac delta function, and the convolution has little effect.

In our implementation, there is a loop in which light curve is convolved with a Gaussian with large variance. Then condition for breaking the loop is checked

$$\left| \int I_{QPP}(t) \mathrm{d}t \right| = \left| \int (I_{tot} - I_{trend}) \mathrm{d}t \right| < \frac{1}{k} \int I_{tot}(t) \mathrm{d}t \tag{A.10}$$

where $k$ is a predefined value, chosen in order to get the right smoothness. If the condition is not satisfied, the loop starts again with lower variance. The results of this method are in Figure A.5 The trends were obtained with the same threshold

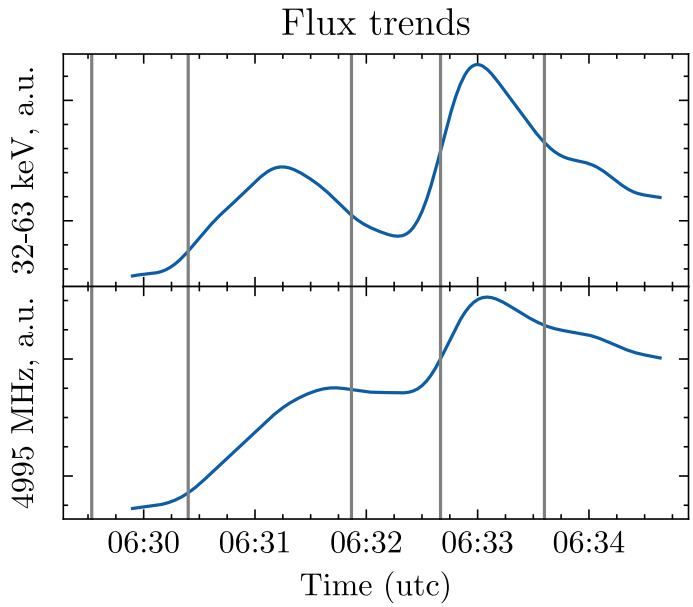


**Figure A.5** Global trends of HXR (top) and radio (bottom) fluxes

$k = 40$.